JCTC Journal of Chemical Theory and Computation

pubs.acs.org/JCTC Article

Unusual Dynamics and Vibrational Fingerprints of van der Waals Dimers Formed by Linear Molecules and Rare-Gas Atoms

Roland Tóbiás, Irén Simkó, and Attila G. Császár*

Cite This: J. Chem. Theory Comput. 2023, 19, 8767−8781 Read Online

ACCESS | Metrics & More | Article Recommendations | Supporting Information

ABSTRACT: Detailed structural, dynamical, and vibrational analyses have been performed for systems composed of linear triatomic molecules solvated by a single rare-gas atom, He, Ne, or Ar. Among the chromophores of these van der Waals (vdW) dimers, there are four neutral molecules (CO_2, CS_2, N_2O, and OCS) and six molecular cations (HHe_2^+, HNe_2^+, HAr_2^+, $HHeNe^+$, $HHeAr^+$, and $HNeAr^+$), both of apolar and polar nature. Following the exploration of bonding preferences, high-level four-dimensional (4D) potential energy surfaces (PESs) have been developed for 24 vdW dimers, keeping the two intramonomer bond lengths fixed. For these 24 complexes, over 1500 bound vibrational states have been obtained via quasi-variational nuclear-motion computations, employing exact kinetic-energy operators together with the accurate 4D PESs and their 2D/3D cuts. The reduced-dimensional (2D to 4D) dimer models have been compared with full-dimensional (6D) ones in the cases of the neutral CO_2·Ar and charged HHe_2^+·He dimers, corroborating the high accuracy of the 2D to 4D vibrational energies. The reduced-dimensional models suggest that (a) while the equilibrium structures are T-shaped and planar, the effective ground-state structures are nonplanar, (b) certain bound states belong to collinear molecular structures, even when they are not minima, (c) the vdW vibrations are heavily mixed and many states have amplitudes corresponding to both the T-shaped and collinear structures, (d) there are a few dimers, for which even some of the vdW fundamentals lie above the first dissociation limit, and (e) the vdW vibrations are almost fully decoupled from the intramonomer bending motion.

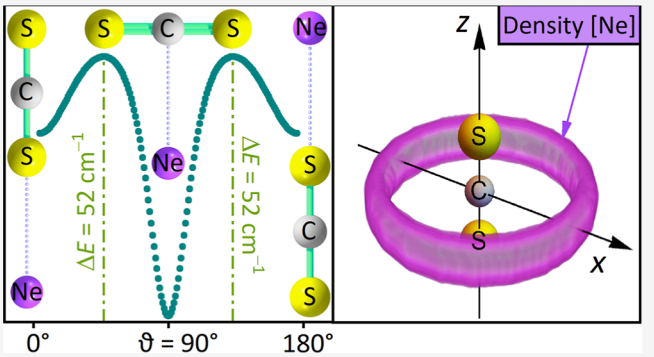

1. INTRODUCTION

In recent studies involving our group,[1−5] interesting structural, dynamical, and spectroscopic results have been reported for the HHe_n^+ and He_n^+ systems, whereby either a proton or a positive charge is "solvated" by He atoms, respectively. In particular, results obtained for HHe_3^+,[5] where a He atom solvates the formally linear HHe_2^+ cation, led us to the present study of the structure, dynamics, and vibrational fingerprints for a collection of van der Waals (vdW) dimers, composed of neutral or charged linear chromophores and a single rare-gas (Rg) atom, Rg = He, Ne, and Ar.

Examining the solvation of neutral polyatomic linear molecules, such as CO_2, CS_2, OCS, N_2O, HCN, C_2H_2, and CNCCH by rare-gas atoms, Rg = He, Ne, Ar, Kr, and Xe, is certainly not a new research topic; a significant amount of structural and spectroscopic information has been gathered for these systems, both via experimental and computational means.[6−77] Many experimental investigations focusing on the interactions of CO_2,[37] OCS,[31,33,43] and N_2O[34] with bosonic ^{4}He atoms have been conducted to understand the so-called microscopic superfluidity phenomenon.[78,79] This effect may also be present in charged species,[1] though it has not been probed experimentally.

There are several publications on proton-bound rare-gas clusters, $H^+Rg^1Rg^2\cdots Rg^n$, as well, especially for n = 1−3; note, in particular, two recent reviews on this topic,[80,81] and the references therein. The species HHe^+, HNe^+, and HAr^+, with strong covalent bonds, act as key intermediates in proton-transfer processes in the interstellar medium. They have recently been detected in various (extra)galactic regions[82−85] (note that HHe^+ is the very first molecule formed during the cooling of the universe). The structures and vibrations of larger HAr_n^+ complexes (n = 3−7) have also been studied via gas-phase infrared spectroscopy.[86] The He-solvated dimers, such as HHe_3^+, HNe_2^+·He, HAr_2^+·He, and $HHeNe^+$·He, have also been playing a crucial role in testing collisional and nonlocal thermodynamic equilibrium models.[87,88] A common structural motif of the four proton-bound rare-gas dimers mentioned is that their chromophores are triatomic, formally linear cations.

Received: August 19, 2023
Revised: November 10, 2023
Accepted: November 13, 2023
Published: November 30, 2023

https://doi.org/10.1021/acs.jctc.3c00914
J. Chem. Theory Comput. 2023, 19, 8767−8781

If a linear molecule, whose quadrupole moment dominates its multipole expansion,[89] interacts with a single solvating atom, the resulting dimer forms a (nearly) T-shaped global minimum (GM), though linear secondary minima (SM) might also be present on the potential energy surface (PES). For apolar centrosymmetric chromophores, such as CO_2, CS_2, and C_2H_2, the GM belongs to the C_{2v} point group. The weakly polar linear chromophores, for instance, those of the ligands OCS and N_2O, produce rare-gas dimers characterized by a GM of C_s point-group symmetry. The most stable structure of a vdW dimer with a highly polar chromophore, such as HCN·Rg, appears to be linear.[90]

In all bound vibrational states of the vdW dimers studied, irrespective of whether they are neutral or charged, the solvating Rg atom exhibits large-amplitude motion of the bend and stretch type, coupled only moderately with the high-frequency vibrations of the strongly bound chromophores. However, owing to the interaction, the high-frequency fundamentals of the chromophores are shifted slightly. As long as a linear chromophore is solvated in a nonlinear fashion, and two new vibrational and one new rotational degrees of freedom are introduced, the intramonomer bending mode loses its two-fold degeneracy. This splits the in-plane (IPB) and the out-of-plane (OPB) bending fundamentals, the extent of which has been studied both experimentally,[72,74,77] and computationally.[76]

This paper is dedicated to the investigation of equilibrium and effective molecular structures, nuclear dynamics, and bound vibrational states of a number of neutral and charged vdW dimers. The set of model systems considered involves dimers of four neutral (CO_2, CS_2, OCS, and N_2O) and six cationic (HHe_2^+, HNe_2^+, HAr_2^+, $HHeNe^+$, $HHeAr^+$, and $HNeAr^+$) linear chromophores with a single solvating atom, Rg = He, Ne, and Ar. Of the 18 formally existing cationic complexes, 6 turn out to be peculiar in one way or another (vide infra), preventing their further investigation. Vibrational characteristics of the 24 remaining dimers have been derived from harmonic analyses,[91] second-order vibrational perturbation-theory (VPT2),[92−94] and reduced-dimensional quasi-variational nuclear-motion computations.[95] In the last case, the exact kinetic-energy operators as well as newly developed four-dimensional (4D) PESs and their 2D/3D cuts are employed, where the intermonomer bond lengths are kept fixed. Nuclear densities, that is the spatial distributions of the nuclei in a body-fixed Cartesian-coordinate system,[5,96] are also obtained for all bound states. To constrain the length of the main text, most of the numerical data are deposited in the Supporting Information, while some technical details are moved to table footnotes and figure captions.

2. COMPUTATIONAL DETAILS

During this study, a large number of high-level electronic-structure and state-of-the-art nuclear-motion computations were executed with the help of several quantum-chemical codes. Joint consideration of the electronic-structure and nuclear-motion quantum-chemical results is needed to understand the structural, dynamical, and spectroscopic properties of the vdW complexes under consideration. In what follows, Rg ∈ {He, Ne, Ar} and $MT'T''$ will designate a solvent atom and a general triatomic chromophore, respectively, where M is the middle, and T' and T'' are the two terminal atoms of the chromophore (for the cationic dimers, the charge is formally assigned to the M = H^+ middle atom).

2.1. Electronic Structure Computations. To yield reference geometries for the single-point energy computations as well as for the harmonic and VPT2 analyses, the geometries of the vdW dimers and their chromophores have been tightly optimized. These computations were executed at the frozen-core MP2[97] and CCSD(T)[98] levels, relying on user-defined triple- (uTZ), quadruple- (uQZ), and pentuple-zeta (u5Z) basis sets. The uXZ bases include (i) the MAX basis functions[4] for H and He, and (ii) the aug-cc-pVXZ[99] basis sets for the other atoms, where X = T(3), Q(4), and P(5). To avoid the nonzero force dilemma,[100,101] the (an)harmonic force constants have been derived at the fully optimized reference structures. Anharmonic computations were carried out at the uQZ CCSD(T) level to ascertain the effective bond lengths and bond angles of the chromophores. Optimizations seeking minima, transition states (TS), and second-order saddle points (SOS), as well as intrinsic reaction-coordinate (IRC)[102,103] computations helped to uncover cases where a dimer does not have a stable T-shaped arrangement.

The MP2 computations were performed with the help of the Gaussian 16 package,[104] while the reference geometries and the anharmonic force fields[105] were obtained at the CCSD(T) level with the code CFOUR.[106,107] To develop 4D PESs for the dimers, the black-box-like autoPES suite of codes,[108,109] interfaced to SAPT,[110,111] MOLPRO,[112] and ORCA,[113] was utilized.

2.2. Construction of 4D PESs. During the generation of the PESs, the bond lengths of the chromophores were frozen at their equilibrium values in the isolated (free) molecule, derived at the uQZ CCSD(T) level (the exception is the HHe_2^+ unit in the HHe_3^+ and HHe_2^+·Ne cations, for which the empirical estimate of the H−He bond length, 0.924 Å,[3] was applied instead of the uQZ CCSD(T) value). All the other variables, namely, the coordinates of the Rg atom and the bond angle of the chromophore, were varied in prescribed ranges.

The configuration space, sampled with weighted randomizing algorithms,[108,109] was split into short-range ($R \le R_{cut}$) and long-range ($R > R_{cut}$) subspaces, whereby R is the M−Rg distance, $R_{cut} \gg R_e$ represents an effective cutoff parameter (not used directly in autoPES), and R_e is the R value in the GM structure. From the short-range subspace, 500−1500 grid points were chosen. These single-point energies were computed at the frozen-core, counterpoise-corrected[114] CCSD(T) level, utilizing the aug-cc-pVTZ and aug-cc-pVQZ basis sets, complemented with midbond functions[115] (the default in autoPES). To provide short-range interaction energies, the single-point energies were extrapolated with formulas advocated in ref 116. In the long-range subspace, where the accuracy requirement is somewhat more relaxed, the interaction energies were obtained, for some 10,000 grid points, via a multipole expansion around the centers of mass of the $MT'T''$ and Rg monomers (see refs 108 and 117).

To increase the flexibility and accuracy of the 4D PESs, off-atomic (OA) sites were specified. The OA positions were optimized simultaneously with the PES parameters, but were restricted to remain on the M−T' or the M−T'' bond, following the intramonomer bending motions. For dimers with T' = T'', (i) an even number of OA sites was adopted, distributed symmetrically on the two sides of the M atom, along the main axis of the chromophore, and (ii) a common parameter set was used for T' and T'' to reflect permutational symmetry (the same holds for the OA pairs placed at identical distances from M). For complexes with Rg ∈ {T', T''}, the

https://doi.org/10.1021/acs.jctc.3c00914
J. Chem. Theory Comput. 2023, 19, 8767−8781

Table 1. Characteristics of the Four-Dimensional PESs Obtained for 24 vdW Complexes, $MT'T''$·Rg, Formed by a Linear Chromophore, $MT'T''$, and a Solvent Rare-Gas (Rg) Atom[a]

		T-shaped structure			nL-type structure			hL-type structure		
complex	RMSD (cm^{-1})	R (Å)	$\mathcal{D}_e$ (cm^{-1})	order	R (Å)	$\mathcal{D}_e$ (cm^{-1})	order	R (Å)	$\mathcal{D}_e$ (cm^{-1})	order
CO_2·He	0.01	3.06	49.9	0	4.26	26.8	0			
CO_2·Ne	0.01	3.14	93.2	0	4.31	53.6	0			
CO_2·Ar	0.02	3.43	198.7	0	4.62	108.6	1			
CS_2·He	0.03	3.38	54.3	0	5.02	32.5	0			
CS_2·Ne	0.06	3.45	103.3	0	5.03	66.9	0			
CS_2·Ar	0.09	3.66	274.9	0	5.26	167.9	0			
OCS·He	0.02	3.20	51.4	0	4.26	28.4	0	4.99	32.88	0
OCS·Ne	0.02	3.28	97.9	0	4.30	56.8	0	5.01	66.70	0
OCS·Ar	0.05	3.54	230.4	0	4.60	119.8	1	5.25	162.65	0
N_2O·He	0.01	2.96	62.6	0	4.45	21.5	0	4.17	32.99	0
N_2O·Ne	0.02	3.10	105.2	0	4.45	46.1	1	4.25	62.91	0
N_2O·Ar	0.03	3.40	220.6	0	4.74	99.2	1	4.56	126.88	0
HHe_3^+	0.15	2.13	354.8	0	3.23	140.9	1			
HHe_2^+·Ne	0.38	2.23	592.6	0	3.32	244.6	1			
HNe_2^+·He	0.04	2.34	265.4	0	3.78	98.9	1*			
HNe_3^+	0.20	2.45	450.2	0	3.90	168.4	1*			
HAr_2^+·He	0.02	2.81	144.3	0	4.54	92.1	0			
HAr_2^+·Ne	0.14	2.87	272.3	0	4.60	171.2	0			
HAr_3^+	0.39	3.17	700.2	0	4.87	444.1	0			
$HHeNe^+$·He	0.08	2.24	299.8	0	3.29	125.7	1	3.73	106.45	1*
$HHeNe^+$·Ne	0.20	2.33	510.8	0	3.38	219.6	1	3.85	180.87	1
$HHeAr^+$·He	0.10	2.42	193.0	0	4.20	39.6	1	4.12	164.16	0
$HNeAr^+$·He	0.08	2.55	181.5	0	4.39	48.1	1	4.16	155.21	0
$HNeAr^+$·Ne	0.14	2.76	331.5	0	4.49	84.8	1	4.24	278.18	0

[a]RMSD denotes the root-mean-square deviation of the fit, utilizing short-range grid points with negative interaction energy. In columns 3−11, quantum-chemical results are provided for the T-shaped and the two linear (nL-type and hL-type, see Section 2.2) SP. For a given SP, (i) R is the M−Rg distance, (ii) $\mathcal{D}_e$ is the dissociation energy, and (iii) "order" is the number of negative Hessian eigenvalues. The orders with asterisks are ill defined due to the extremely flat PES. For dimers with $T' = T''$, the two linear structures are equivalent; the related data are given as "nL-type".

exchanges $T' \leftrightarrow$ Rg and/or $T'' \leftrightarrow$ Rg are allowed by symmetry, but this effect is ignored here. However, this constraint does not influence the computed vibrational energies of the bound states in any significant way.

Table 1 summarizes the most important characteristics of the 4D PESs created by the autoPES code for 24 dimers. An explanation why the six dimers, HHe_2^+·Ar, HNe_2^+·Ar, $HHeNe^+$·Ar, $HHeAr^+$·Ne, $HHeAr^+$·Ar, and $HNeAr^+$·Ar, are not included in Table 1 is offered in Section 3. Beyond the goodness of the fits (see column "RMSD"), Table 1 also gives information about three particular stationary points (SP): the T-shaped GM and the two linear arrangements. If T'' is heavier than T', the $T'-M-T''\cdots$Rg configuration is called hL-type; otherwise, it is named nL-type, where h/n refers to "heavier"/normal. This notation is not precise for dimers with $T' = T''$, where the two linear arrangements are equivalent.

For the global minima of the species investigated, both for the dimers and their chromophores, all the results derived from the 4D PESs and from direct electronic-structure computations are presented in Tables S1−S3 of the Supporting Information. The PES parameter files, together with a Fortran code calculating the interaction energy at a specific geometry, are also given in Supporting Information.

2.3. Quasi-Variational Nuclear-Motion Computations.

Relying on our in-house code GENIUSH,[118−120] first-principles, quasi-variational nuclear-motion computations were performed for numerous reduced-dimensional vibrational models. These models delivered bound-state vibrational energies for the most abundant isotopologues of 24 vdW dimers, making use of masses defined in Table S4.

To produce converged results, a large number of GENIUSH computations had to be executed for the 24 dimers, although in a mostly automated fashion. During these computations, a valence-type coordinate system, displayed in Figure 1, was

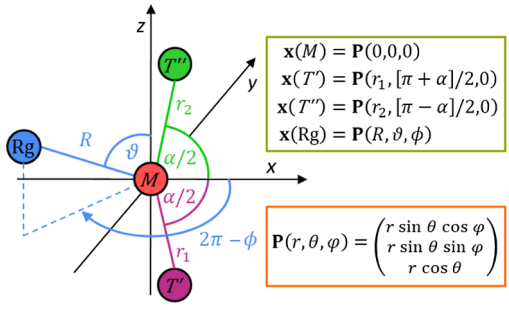

Figure 1. Valence-type internal-coordinate system employed for the $MT'T''$·Rg complexes. The (r_1, r_2, α, R, ϑ, ϕ) sextuplet stands for the valence-type coordinates, specified in the usual way with lines and arcs. In the olive box, the Cartesian positions of an atom A, $\mathbf{x}(A)$, are expressed with the $\mathbf{P}(r, \theta, \varphi)$ function (see the orange box), whereby the (r, θ, φ) triplet stands for spherical polar coordinates (following the convention utilized in Figure 6.3 of ref 122). Instead of ϕ, the conjugate angle, $2\pi - \phi$, is displayed in this figure.

https://doi.org/10.1021/acs.jctc.3c00914
J. Chem. Theory Comput. 2023, 19, 8767−8781

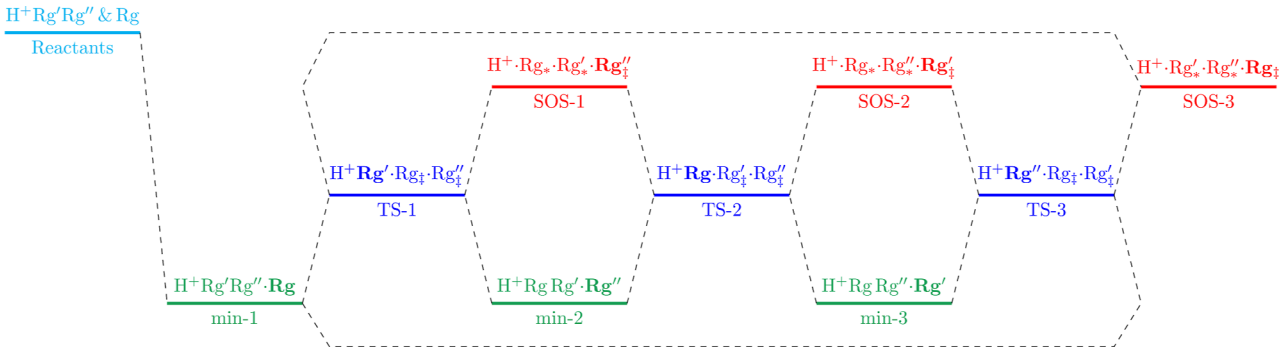

Figure 2. Cartoon illustrating the exchange of rare-gas atoms within an arbitrary [H, Rg, Rg′, Rg″]$^+$ vdW complex. Depending on whether Rg, Rg″, or Rg′ play the role of the (boldfaced) solvent atom, three different minima can be specified, min-1, min-2, and min-3, respectively. When two rare-gas atoms exchange places, they are farther from H^+ in the transition state (TS) than the third ("passive") rare-gas atom, which remains strongly bonded to the proton. In TS-1, TS-2, and TS-3, the passive atom, shown in boldface, is Rg′, Rg, and Rg″, respectively. Subscript ‡ designates an "activated" rare-gas atom, whose role is different in the TS and the minimum. Three second-order saddle points, SOS-1, SOS-2, and SOS-3, may also appear, where all three rare-gas atoms form a noncovalent bond with H^+. In these SOSs, at least two atoms, denoted with an asterisk, are closer to the proton than in the TSs. In the presence of permutational symmetry, certain min/TS/SOS configurations have identical energy.

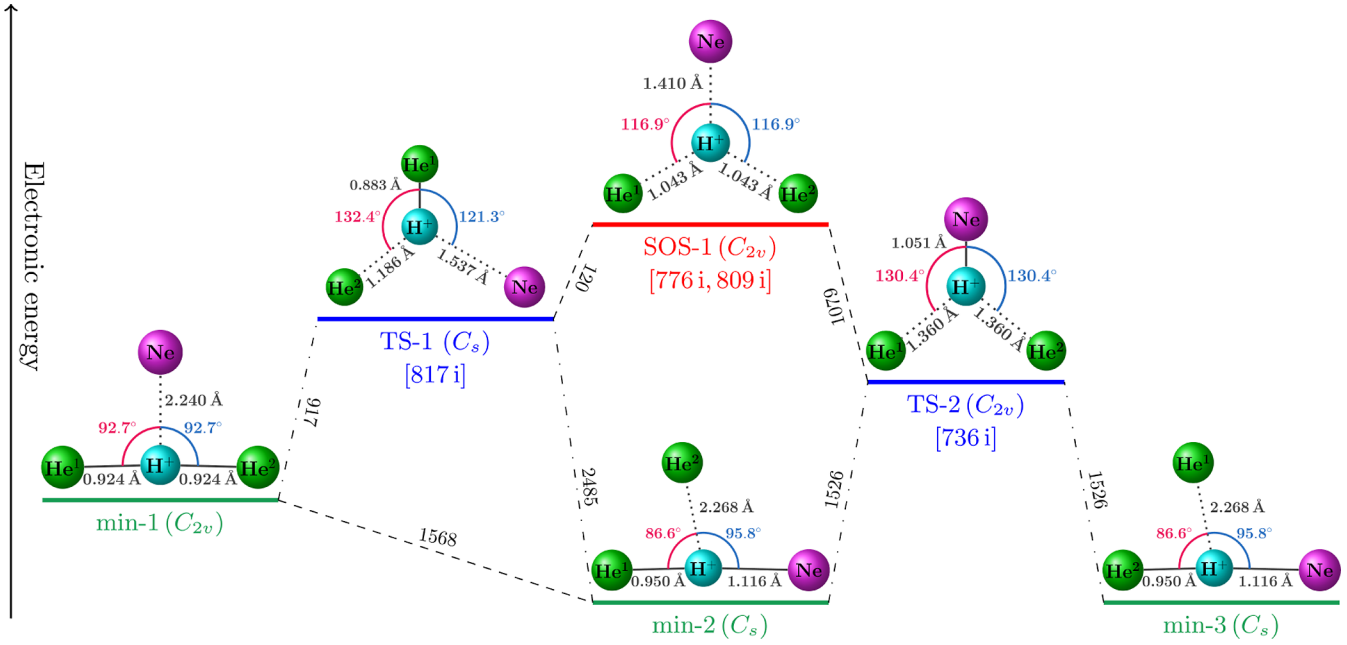

Figure 3. Schematic energy diagram for the exchange of rare-gas atoms within the [H, He, He, Ne]$^+$ vdW complex. Of the three minima, min-2 and min-3 are permutational isomers. Regarding the two nonequivalent transition states, (a) TS-1 describes a He → Ne exchange in HHe_2^+·Ne, and (b) TS-2 links the HHe^1NeHe^2 and HHe^2NeHe^1 permutational isomers, where superscripts 1 and 2 distinguish the two He atoms. TS-3, which is equivalent to TS-1, is not shown here. No TS could be identified between those of HHe^1He^2Ne and HHe^2He^1Ne. The PES also contains two equivalent second-order saddle points, SOS-1 and SOS-3, and only SOS-1 is displayed. An SOS-2 configuration, expected between TS-1 and TS-2 and characterized with two different H−He distances, could not be found. The point groups of these six SP are provided in parentheses. The integers on lines connecting SPs are electronic energy differences in cm^{-1}, determined at the uQZ MP2 level. The imaginary harmonic fundamentals in parentheses and the internal coordinates on the molecular drawings are also uQZ MP2 values. Each covalent/secondary bond is given as a solid/dotted line. The dash-dotted lines represent minimum-energy paths computed at the uTZ MP2 level.

used. For each active coordinate, DVR (discrete variable representation)[121] basis functions were employed, from which a direct-product vibrational basis was assembled (see Table S5 for the DVR basis types and the associated coordinate ranges).

The energies of the bound states were refined iteratively, increasing the DVR basis for each coordinate until convergence was reached within a prescribed τ tolerance. The τ value was selected to be (a) 0.15 cm^{-1} for the cationic complexes, (b) 0.1 cm^{-1} for CS_2·Ne and CS_2·Ar, and (c) 0.05 cm^{-1} for all of the other neutral dimers. The initial R range was specified as the largest $[R_{low}, R_{up}]$ range, for which $|v(R_{low})| \leq 50\,\mathcal{D}_e$ and $|v(R_{up})| \geq 0.01\,\mathcal{D}_e$, where $\mathcal{D}_e$ and $v(R)$ symbolize the dissociation energy and the 1D-R cut of the PES at the GM, respectively. This range was then decreased, while the vibrational energies remained converged. As a simple empirical rule, the highest-energy state with $d(R_{up}) > 0.05d^*$ was treated as the last bound state in all computations, whereby (a) $d(R)$ is the reduced 1D-R wave function density at a specific R value, and (b) d^* is the largest $d(R)$ value on the actual coordinate grid. This criterion is justified by the fact that the eigenfunctions of the unbound states start to resemble the particle-in-a-box wave functions, without decaying at the end

https://doi.org/10.1021/acs.jctc.3c00914
J. Chem. Theory Comput. 2023, 19, 8767−8781

of the R range. For the final bound-state vibrational energies, statistical uncertainties were derived from 10 computations by randomly perturbing the optimal R range and basis size.

For the vibrational bound states, the expectation values of the internal coordinates are calculated in the valence-type coordinate system shown in Figure 1. For symmetry reasons, (i) ϕ and $2\pi - \phi$ are equivalent for all dimers, while (ii) ϑ and $\pi - \vartheta$ are equivalent for dimers with $T' = T''$. Cases (i) and (ii) can be handled by the redefinitions $\langle\phi\rangle := \langle\min(\phi, 2\pi - \phi)\rangle$ and $\langle\vartheta\rangle := \langle\min(\vartheta, \pi - \vartheta)\rangle$, respectively, whereby $\langle\cdot\rangle$ is the expectation-value operation (otherwise the expectation values of ϕ and ϑ would be π and $\pi/2$, respectively). For coordinate $c \in \{r_1, r_2, \alpha, R, \vartheta, \phi\}$, (i) the equilibrium value is designated with c_e, (ii) the expectation value in the ground vibrational state is denoted as c_0, and (iii) the value in the isolated chromophore is given as $\tilde{c}$.

Using the vibrational eigenfunctions determined, nuclear densities of the atoms, in body-fixed coordinates, are calculated to (i) help the assignment of the vibrational states and (ii) visualize nuclear delocalization and the dynamical structure of the complexes (for technical details, see ref 96). Body-fixed nuclear densities describe the spatial distribution of nuclei in a body-fixed Cartesian coordinate system (embedding). Such an embedding has to be chosen to specify the $3N$ Cartesian coordinates of an N-atomic species, as the $3N - f_{ext}$ internal coordinates are insufficient, where f_{ext} is the number of external (translational and rotational) degrees of freedom. For a given molecule, many sensible embeddings can be selected; this choice strongly influences the appearance of the nuclear density and, thus, its interpretation. This study employs the embedding presented in Figure 1, suitable to illustrate the delocalization of the solvent atom around the quasilinear chromophore.

3. BONDING PREFERENCES

To explore the bonding characteristics of the vdW complexes considered, SPs were searched for on the uTZ and uQZ MP2 PESs. The T-shaped GMs were also optimized at the uQZ CCSD(T) level. IRC computations performed at the uTZ MP2 level aided in connecting the minima to the TSs. The results of our extensive analysis agree with earlier findings,[24,30,35,39,40,49,52,58,67,70,123] in the sense that the main structural changes are due to (i) the mobility of H^+ in the charged dimers[123] and (ii) the internal rotation of the Rg atom in both the neutral and the charged species.

Figure 2 shows a cartoon for the proton-mobility-driven exchange of rare-gas atoms within a formal $[H, Rg, Rg', Rg'']^+$ dimer. A representative example for such exchanges, involving the $[H, He, He, Ne]^+$ dimer, is given in Figure 3. Similar exchange schemes for the other charged systems are given in the Supporting Information (see Figures S1−S6). Our detailed computations led to three general observations: (i) all SPs shown in Figure 2 exist for the HRg_3^+ dimers, (ii) the significant energy gain due to the formation of a H−Ar covalent bond means that the T-shaped HHe_2^+·Ar, $HHeNe^+$·Ar, $HHeAr^+$·Ar, and $HNeAr^+$·Ar isomers do not exist (similarly, the $HHeAr^+$·Ne isomer is nonexistent due to a He ↔ Ne exchange), and (iii) the H−Y bond of $HYAr^+$, whereby Y is He or Ne, can be interpreted as a quasi-covalent ("half") bond, because it lies halfway between the covalent and the vdW bonds in terms of strength (for details, see Figure S7 and ref 80). It should also be noted that (i) there is no SOS with a covalent H−He bond for $[H, He, He, Ne]^+$, (ii) the existing SPs of $[H, He, Ne, Ne]^+$, for which HNe_2^+·He is the more stable form, involve at least one covalent H−Ne bond, and (iii) though the HNe_2^+·Ar isomer with two covalent H−Ne bonds is stable, its complicated IRC profile (see Figure S5) explains why no reliable PES could be deduced for this isomer. In what follows, 24 isomers, separated with high barriers from other isomers, are considered (they are listed in Table 1).

The SPs due to the motion of the Rg atom represent T-shaped, linear, and "skewed" ($\vartheta \approx 45°$) structures, whose coordinates extracted from our 4D PESs are listed partly in Table 1 and fully in Table S6. The skewed SPs are always TSs and link the linear and T-shaped isomers on the 4D PESs, while the linear saddle points connect the two versions of T-shaped GMs with $\phi = 0°/180°$. These linear saddle points are TSs or SOSs, depending on whether ϕ, which is redundant for $\vartheta = 0°$ and $\vartheta = 180°$, is ignored or not (in this paper, they are handled as TSs). Interestingly, linear TSs appear even for charged dimers with unstable T-shaped GMs (Table S7).

4. ASSESSMENT OF THE REDUCED-DIMENSIONAL MODELS

For the quasi-variational vibrational analyses of the present study, six reduced-dimensional models (Table 2) have been utilized. The two 4D models are able to treat the intermonomer vibrations of these and similar solvated complexes, as the two intramonomer stretch motions can be meaningfully decoupled from the remaining modes (they have quite different time and energy scales).

Table 2. Specification of the nD (n = 2, 3, 4, and 6) Vibrational Models Utilized During this Study[a]

model	r_1	r_2	α	R	ϑ	ϕ
6D	A	A	A	A	A	A
$4D^e$	F{$\tilde{r}_{1,e}$}	F{$\tilde{r}_{2,e}$}	A	A	A	A
$4D^0$	F{$\tilde{r}_{1,0}$}	F{$\tilde{r}_{2,0}$}	A	A	A	A
$3D^e$	F{$\tilde{r}_{1,e}$}	F{$\tilde{r}_{2,e}$}	F{178°}	A	A	A
$3D^{e,0}$	F{$\tilde{r}_{1,e}$}	F{$\tilde{r}_{2,e}$}	F{α_0}	A	A	A
$2D^e$	F{$\tilde{r}_{1,e}$}	F{$\tilde{r}_{2,e}$}	F{178°}	A	A	F{ϕ_e}
$2D^{e,0}$	F{$\tilde{r}_{1,e}$}	F{$\tilde{r}_{2,e}$}	F{α_0}	A	A	F{ϕ_0}

[a]The first column contains the labels denoting the reduced-dimensional vibrational models. The other columns indicate whether a given valence-type internal coordinate is active (A) or frozen (F) within the model. Parameters in braces designate at which value a specific coordinate is fixed ($\tilde{r}_{1,e}$, $\tilde{r}_{2,e}$, $\tilde{r}_{1,0}$, and $\tilde{r}_{2,0}$ are defined in the fourth paragraph of Section 2.3). To avoid coordinate ϕ to be ill determined, the angle α is frozen at 178° instead of 180° in the $4D^e$ and $3D^e$ models. See Figure 1 for the definition of the valence-type internal coordinates.

Of the 24 complexes seen in Table 1, full-dimensional (6D) PESs exist in the literature for the neutral CO_2·Ar[76] and the charged HHe_3^+[5] dimers. The quasi-variational results based on these two 6D PESs are used to validate the accuracy of our 2D, 3D, and 4D models. Furthermore, computational results relying on 4D cuts of the 6D PESs are checked to see whether the $4D^e$ or the $4D^0$ model is able to better reproduce the reference 6D vibrational energies. The lower-dimensional (LD) $3D^e$, $3D^{e,0}$, $2D^e$, and $2D^{e,0}$ models help to evaluate the influence of the α and ϕ coordinates (see Figure 1) on the vibrational energies.

4.1. Test Cases. *4.1.1. Test Case I: CO_2·Ar.* For the CO_2·Ar dimer, the first 15 vdW vibrational states have been

https://doi.org/10.1021/acs.jctc.3c00914
J. Chem. Theory Comput. 2023, 19, 8767−8781

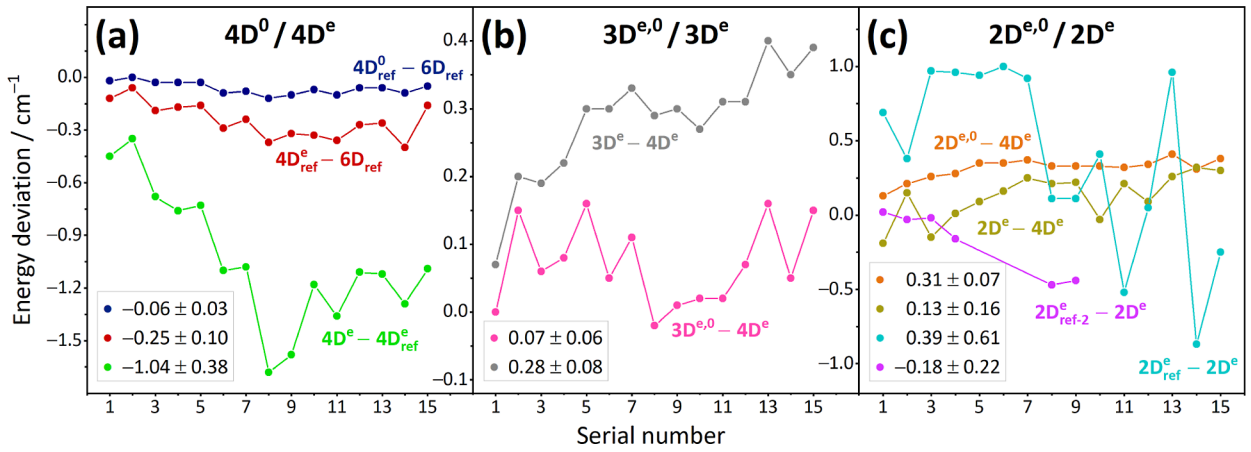

Figure 4. Graphical comparison of the vibrational energies obtained with different models for the CO_2·Ar dimer. The models applied to deduce the vibrational energies of the first 15 vdW states are listed in Table 2. The horizontal axes present the serial numbers of the states in increasing energy order, while the vertical axes show the vibrational-energy deviations associated with certain model pairs. These model pairs are indicated separately for every curve. In the gray-framed boxes, the average differences and their standard deviations, in cm^{-1}, are displayed for all data sets. The results of models indexed with "ref" were produced in this study, utilizing the PES of ref 76, whereas the $2D^e_{ref\text{-}2}$ vibrational energies were taken from ref 69. For further information, see the footnote to Table S8.

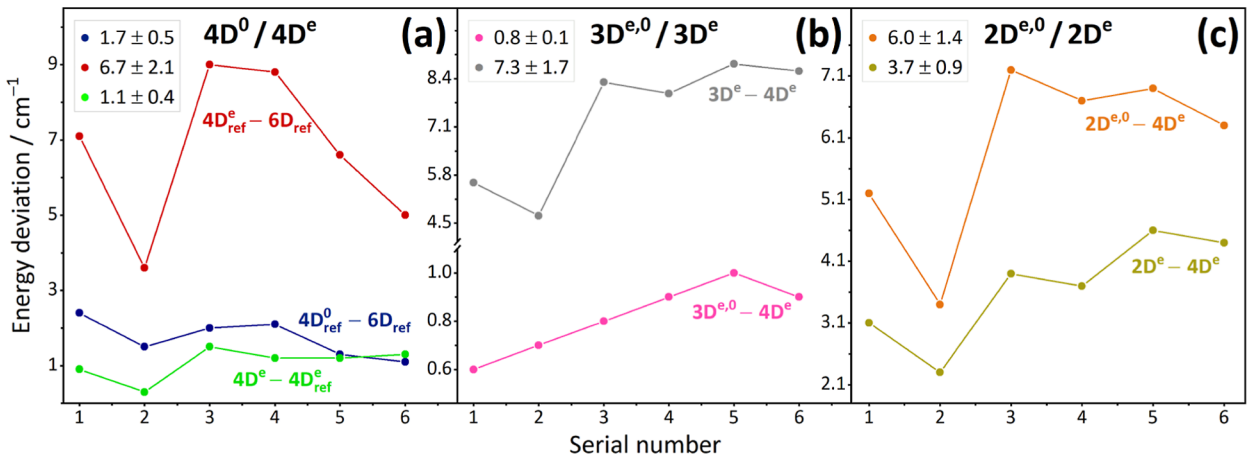

Figure 5. Graphical comparison of the vibrational energies determined with different models for the HHe_3^+ dimer. This figure follows the format and the notation of Figure 4, but subscript "ref" now designates the results of ref 5. The comparison is performed for the first six vdW vibrational states, whose energies fall below the first dissociation limit reported in ref 5. For additional details, see the footnote to Table S9.

determined with the seven models of Table 2. The 6D computations took advantage of a PES[76] that was fitted to aug-cc-pVTZ CCSD(T)-F12b interaction energies without counterpoise correction. In these 6D computations, nine Hermite-type basis functions were employed for the r_1 and r_2 coordinates (see Figure 1), sufficient to extract the intramonomer stretch fundamentals within a few cm^{-1}. These two stretch coordinates were constrained to the range of [1.0,1.4] Å. For the other coordinates, bases optimized for the $4D^e$ model were adopted (the R range, [3.0,5.1] Å, was also chosen based on the $4D^e$ model). Each model used the same R interval and the same number of basis functions for the active coordinates. Convergence of the 6D and 4D results was carefully checked, revealing a precision better than 0.06 cm^{-1} for the final energies. The deviations among the various models utilized are plotted in Figure 4.

First, let us compare the performance of our 4D PES to literature results from refs 69 and 76. The vibrational energies computed with our 4D PES differ, with the same sign, by 0.3−1.7 cm^{-1} from those derived via the potential of ref 76 (green in Figure 4a). Since our 4D PES represents a higher level of electronic-structure theory (see Section 2.2), these small, systematic deviations may be due to basis set superposition error (BSSE), not treated in the PES reported in ref 76. In the $2D^e$ case (turquoise in Figure 4c), the differences are also small but not systematic. Note that the results generated with our 4D PES show better agreement with the first-principles data of ref 69 (violet in Figure 4c), where the PES was corrected for BSSE.

As the deviations observed in the $4D^e_{ref}$ and $4D^e$ cases are small, the 6D PES of ref 76 can be applied safely to ascertain the impact of the 6D → $4D^e$/$4D^0$ reduction on the vibrational energies. Utilizing the 4D cut of the 6D reference PES, subtle and nearly constant shifts can be seen in the $4D^e$ vibrational energies when compared to the 6D results (red in Figure 4a). Furthermore, these $4D^e$−6D differences are consistently larger than the $4D^0$−6D ones (blue in Figure 4a). Hence, freezing r_1 and r_2 at the effective r_0 value instead of r_e slightly improves the accuracy of the vibrational energies extracted from a 4D model.

Looking at the LD models, the results produced with the $3D^{e,0}$ model agree best with their $4D^e$ counterparts (pink in Figure 4b), exhibiting a minuscule average deviation. The

https://doi.org/10.1021/acs.jctc.3c00914
J. Chem. Theory Comput. 2023, 19, 8767−8781

Table 3. Excerpt of Quasi-Variational Results Obtained for Bound States of 24 vdW Complexes[a]

complex	previous studies	#bound	$\overline{\mathcal{D}}_0$	T-bend	T-stre	nL-GS	nL-bend	nL-stre	hL-GS	hL-bend	hL-stre
CO_2·He	24,47,48	4	13			8.3	13.0		[1.15]		
CO_2·Ne	52	18	57	17.5	22.8	26.6	31.3	46.9	[0.60]	[0.97]	[0.78]
CO_2·Ar	49,69,76	58	154	27.6	34.1	72.6	78.7	100.0	[0.24]	[1.01]	[0.28]
CS_2·He	65,67	7	19	12.4		10.9	17.3		[0.10]	[1.43]	
CS_2·Ne	62,67,68	44	73	16.1	23.3	30.0	37.7	51.1	[0.02]	[1.00]	[0.04]
CS_2·Ar	59,64,67	192	237	24.8	34.7	97.2	109.0	126.4	[0.01]	[0.07]	[0.01]
OCS·He	26,58	6	17	12.3		8.9	14.5		9.1	17.3	
OCS·Ne	25,39	27	63	15.9	23.6	30.7	36.1	50.5	24.3	34.6	45.8
OCS·Ar	40,61	112	190	24.6	34.9	94.0	102.8	120.8	59.5	75.8	89.6
N_2O·He	35,36,45	5	19			14.2	19.3		12.1	17.4	
N_2O·Ne	30	19	65	22.1	26.6	40.7	46.8	58.3	30.4	37.3	52.5
N_2O·Ar	70,71	65	175	32.4	36.9	97.9	105.2	121.6	76.8	80.2	106.7
HHe_3^+	5	10	197	88	98	134	163	192	[0.6]	[2.0]	[5.5]
HHe_2^+·Ne		29	426	124	111	282	326	337	[3.1]	[1.1]	[3.1]
HNe_2^+·He		20	160	51	70	116	136	155	[4.5]	[3.5]	[0.0]
HNe_3^+		88	353	56	67	232	244	277	[0.1]	[0.5]	[0.6]
HAr_2^+·He		22	82	26	50	36	42	73	[0.2]	[2.1]	[0.4]
HAr_2^+·Ne		152	225	30	42	88	100	127	[0.0]	[0.1]	[0.0]
HAr_3^+		619	631	41	53	239	259	286	[0.0]	[0.0]	[0.0]
$HHeNe^+$·He		14	171	61	81	117	147	167	126	150	171
$HHeNe^+$·Ne		48	366	66	101	216	235	282	261	284	308
$HHeAr^+$·He		13	96	34		96			14	40	73
$HNeAr^+$·He		18	100	31		88	94		17	37	74
$HNeAr^+$·Ne		90	244	37	51	207	213	236	41	66	95

[a]The number of bound vibrational states, #bound, corresponds to the $4D^e$ and $3D^e$ models for the first 14 and the last 10 complexes, respectively. The largest bound-state energy, $\overline{\mathcal{D}}_0$, gives an estimate for the $\mathcal{D}_0$ dissociation limit. Columns 5−12 report $4D^e/3D^e$ vibrational energies relative to the T-GS states, as well as tunneling splittings in brackets, for eight vdW states, specified in cm^{-1}. The *S*-GS, *S*-bend, and *S*-stre labels designate the ground state, the vdW bend fundamental, and the vdW stretch fundamental of the *S* structure, respectively, where *S* is T-shaped, nL-type, or hL-type. Each underlined energy denotes a state for which the chosen label is only partially correct (this is especially true for states where the underlying nuclear configurations are saddle points, see also Section 6.3). The missing vdW fundamentals are outside the sets of bound states.

effect of inactivating the α angle is quantified by the $4D^e-3D^e$ differences (gray in Figure 4b), indicating a systematic shift in the $3D^e$ vibrational energies. For the $2D^{e,0}$ and $4D^e$ models, orange and olive in Figure 4c, respectively, similar deviations are found as in the two 3D cases.

4.1.2. Test Case II: HHe_3^+. The accuracy of the six reduced-dimensional models, exploiting our 4D PES and its LD cuts, was also evaluated against 6D, $4D^e$, and $4D^0$ quasi-variational results reported for HHe_3^+.[5] These reference computations involved a 6D PES obtained at the aug-cc-pVQZ-OPTRI DF-CCSD(T*)-F12b level,[5] supposedly delivering an accuracy better than 1 cm^{-1} for the vibrational energies. A comparison of the results is given in Table S9 and Figure 5.

The conclusions one can draw for the case of HHe_3^+ are basically the same as those already given for CO_2·Ar. The essential difference is that the deviations among the individual models are larger for HHe_3^+ than for CO_2·Ar, in accordance with the higher dissimilarity between $\tilde{r}_e$ (0.924 Å) and $\tilde{r}_0$ (0.968 Å) of HHe_2^+. As to the $6D-4D^0$, $6D-4D^e$, $4D^e-3D^{e,0}$, and $4D^e-3D^e$ differences, blue, red, pink, and gray lines in Figure 5, respectively, their average values imply once again that r_1/r_2 and α should preferably be fixed at their vibrationally averaged values. Nonetheless, for the purposes of this investigation, the uncertainty of the $4D^e$ model, 5−10 cm^{-1}, is considered to be good. At this level of accuracy, the deviations between the $4D^e$ results of the present study and those of ref 5 (green in Figure 5a) are deemed insignificant. Similar to the CO_2·Ar case, the $4D^e \rightarrow 2D^{e,0}$ replacement does not improve the computed vibrational energies.

4.2. General Implications. Based on the extensive tests of Section 4.1, it is expected that our 2D to 4D models yield vibrational energies with an uncertainty of 1−2 cm^{-1} and 5−10 cm^{-1} for the neutral and charged complexes of Table 1, respectively. While attempts have been made to employ 4D models for the computation of IPB/OPB energies, as well, the accuracy of these results proved to be unsatisfactory for HHe_3^+. Thus, further analysis is required to find an accurate reduced-dimensional model for the IPB/OPB fundamentals, which is beyond the scope of the present study. Next, two relevant modeling aspects are considered; both may affect the accuracy of the (ro)vibrational models.

Our study confirms that it is important to know how the chromophore's structure is treated during the creation of reduced-dimensional PESs and the subsequent vibrational computations. Whenever the effective and equilibrium structures are considerably different, there may be large discrepancies in the vibrational energies. To decide how to fix an internal coordinate c in the chromophore, VPT2 results[94] may provide assistance to the modelers. If $|\tilde{c}_0 - \tilde{c}_e|$ is large, then (i) c should be fixed at $\tilde{c}_0$ instead of $\tilde{c}_e$, or (ii) one might need to include c in the vibrational model. An example for case (ii) is the bond-angle coordinate of the cationic dimers (see Table S10), where $\tilde{\alpha}_0$ differs from $\tilde{\alpha}_e = 180°$ by 15−20°. When the effective bond/torsion angles of the chromophore are not accessible from VPT2 computations, their values can be estimated from the interatomic distances with an accuracy of a few degrees.

https://doi.org/10.1021/acs.jctc.3c00914
J. Chem. Theory Comput. 2023, 19, 8767−8781

Before generating a PES, it is also necessary to investigate whether multiple structural isomers are present or not. This issue occurs here, for example, for the $[H, He, He, Ne]^+$ system with isomers HHe_2^+·Ne and $HHeNe^+$·He (see also Section 3). In a full-dimensional treatment, the interaction of such isomers should be accounted for to achieve accurate results. However, this interaction can be safely neglected in reduced-dimensional models sampling the geometric space around only one isomer (in fact, our 2D to 4D models satisfy this criterion).

5. REDUCED-DIMENSIONAL VIBRATIONAL RESULTS

For the bound vibrational states of the 24 dimers listed in Table 1, quasi-variational nuclear-motion computations have been performed for the $2D^e$, $2D^{e,0}$, $3D^e$, and $3D^{e,0}$ models. The $4D^e$ model has been employed exclusively for HHe_3^+, HHe_2^+·Ne, and the 12 neutral dimers (class A), because it is not adequate for the other complexes (class B). In class A, the isolated chromophore's fundamentals reflect the expected energy ordering, STRE-I > STRE-II > BEND, whereas the order of STRE-II and BEND is reversed in class B. This suggests that STRE-II may have a larger effect on the vdW states of class B dimers than the BEND state. In consequence, $4D^e/3D^e$ is treated here as the best model for class A/B.

The final vibrational energies, obtained with the best model and augmented with state-by-state statistical uncertainties (see Section 2.3), are given in the Supporting Information as part of separate files for each dimer. The results of the other 2D/3D models, whose deviations from the best energies may help to judge the real computational accuracy, are also listed in these files. Ground-state energies of these reduced-dimensional models are not reported, as they are not useful for practical purposes. From the vibrational results obtained, an excerpt is presented in Table 3, where the second column lists previous first-principles investigations for the neutral complexes and for HHe_3^+. Most studies dealing with neutral dimers employed 2D models, where R and ϑ were the only active variables.

From the numerical data of Table 3, one can deduce the following observations: (i) except for HHe_2^+·Ne, T-bend lies below T-stre on the energy scale, (ii) the T-bend energy is usually smaller than the nL/hL-GS energies (apart from some weakly bound He-solvated dimers), (iii) certain vdW fundamentals are not bound states, as found in refs 47 and 65 for CO_2·He and CS_2·He, and (iv) a tunneling effect occurs when the two linear forms are equivalent, leading to pronounced tunneling splittings. Due to the systematic nature of the $4D^e$ and $3D^e$ model errors (see Section 4.1), these splittings are more accurate than the vibrational energies themselves.

6. EFFECTIVE STRUCTURES AND NUCLEAR DENSITIES

Beyond vibrational energies, nuclear densities of the solvent Rg atoms were also computed with the best $4D^e/3D^e$ models (see also Section 2.3). In this section, these densities are utilized to examine the effective structures of the bound vibrational states, as well as the presence of various couplings in these states. Our discussion first considers the T-GS ("absolute") ground states, then the excited vdW vibrations are analyzed in two separate subsections, making a practical distinction between "pure" (very-weakly mixed) and heavily-mixed states. Out of the large number of excited vdW vibrations, only the characteristic states listed in columns 5−10 of Table 3 will be investigated in detail.

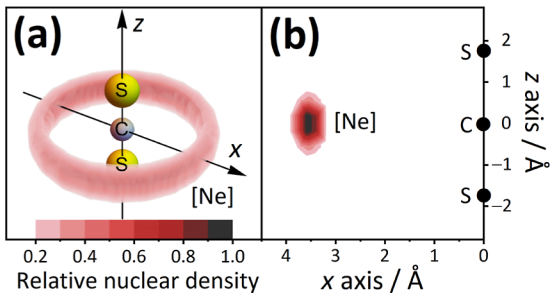

Figure 6. Nuclear-density-based representations for the ground-state structure of the CS_2·Ne vdW dimer. Panel (a) shows a three-dimensional (3D) nuclear density, forming a torus around the center of the CS_2 chromophore, calculated in the body-fixed frame of Figure 1. Panel (b) is a 2D cut of panel (a), determined by integrating the 3D density along ϕ (see Figure 1). For convenience, the CS_2 chromophore is shown in its equilibrium (linear) structure. The color palette at the bottom of panel (a) indicates the values of the relative nuclear densities obtained by dividing the density values by the maximum density. Relative densities below 0.2 are not plotted.

6.1. Ground Vibrational State. Figure 6 shows the 3D and 2D nuclear densities of the Ne atom in the ground vibrational state of the CS_2·Ne complex. All the other dimers studied exhibit similar densities for the solvent atoms, as illustrated in Figures S8 and S9. The message of these density plots is that the effective structure is three-dimensional, thus vastly different from the planar, T-shaped equilibrium geometry. Although this effective structure was first observed for HHe_3^+,[5] the present study proves that the toroidal shape, in the embedding selected, is a general property of the 24 vdW complexes. It must be stressed that (i) this torus-like delocalization is *not* caused by the overall rotation of the dimers, as the nuclear densities are calculated with purely vibrational wave functions, and (ii) alternative embeddings would provide significantly different density distributions.

Delocalization of the solvent Rg atom in the vdW dimers studied can be explained as follows. In its ground vibrational state, the triatomic chromophore bends in the xz plane (Figure 6a), and once it is bent, the ϕ angle (see Figure 1) uniquely describes the internal rotation of the Rg atom in the xy plane. The potential along ϕ is extremely shallow, creating an almost barrierless circular potential well; therefore, the nuclear wave function is able to delocalize in this well, inducing a torus-shaped density (for details, see refs 5 and 19). The thickness of this torus changes with ϕ, but this effect remains minuscule for the 24 dimers. In order to simplify the figures, 2D density plots will be given in Sections 6.2 and 6.3 for the nuclear-density analysis of the excited vibrational states.

6.2. Pure Excited Vibrations. As shown in Figures 7a−c, S10, and S11, the nuclear densities form double tori for the pure T-bend states, where the two tori are divided by a nodal surface perpendicular to the bent chromophore's plane. The results shown for CO_2·Ne (Figure 7b) and OCS·Ar (Figure 7c) corroborate findings documented in ref 5 for HHe_3^+ (see also Figure 7a). For the same chromophore, the thickness of these tori decreases with the size of the solvating atom, just as expected. Around the chromophores with $T' \neq T''$, the placement of the tori is strongly asymmetric, except for N_2O·Rg, where the terminal atoms have very similar Merz−Kollman[124,125] charges (−0.304 e for N and −0.288 e for O, obtained at the uTZ MP2 level).

https://doi.org/10.1021/acs.jctc.3c00914
J. Chem. Theory Comput. 2023, 19, 8767−8781

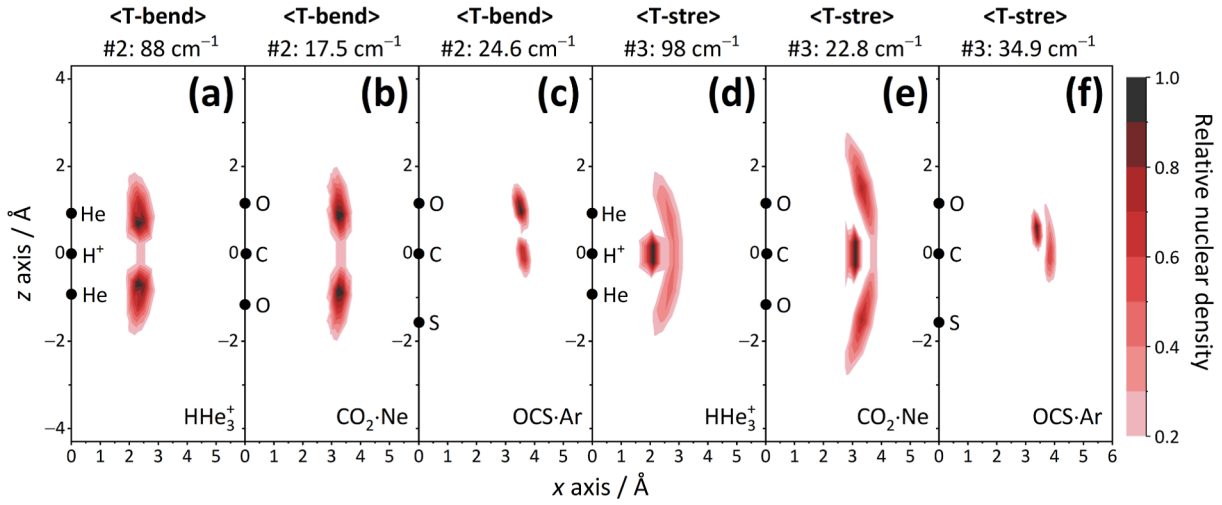

Figure 7. Nuclear densities of the solvating atoms in the *xz* plane for selected vdW states of T-shaped arrangements. Panels a–c and d–f depict "pure" vdW bend and stretch fundamentals, respectively, corresponding to dimers with three different chromophores and three different Rg atoms. The vibrational energies and assignments are displayed at the top of the panels along with the state counting numbers. For further details, see the caption to Figure 6.

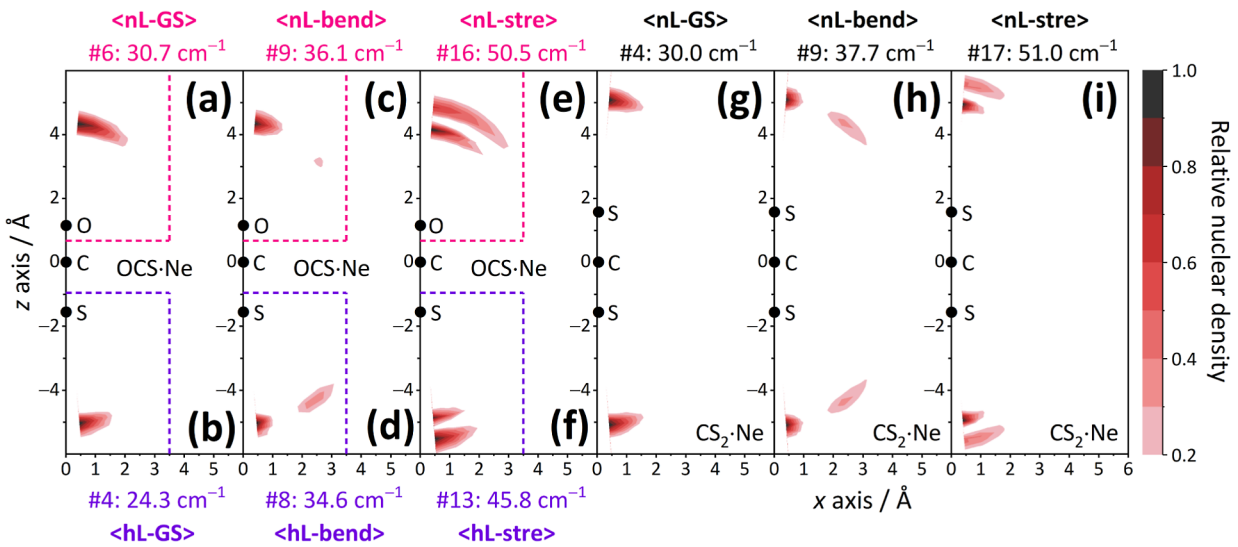

Figure 8. Nuclear densities of the solvating atoms in the *xz* plane for selected vdW states of linear configurations. For panels g–i, the same convention is employed as in Figure 7, while panels (a), (c), and (e) are contracted here with panels (b), (d), and (f), respectively. This contraction is allowed by the fact that there is no significant density outside the pink and violet dashed borders for the nL- and hL-type arrangements of the OCS·Ne dimer, respectively. For panels (b), (d), and (f), the state counting numbers, the vibrational energies, and the vibrational assignments are placed below the horizontal axes. For further details, see the caption of Figure 6.

A double toroidal structure can also be discerned for the pure T-stre states (see Figure 7d–f), where the outer shell of the density is significantly more elongated than the inner one. For a specific chromophore, the two tori shrink with the size of the Rg atom, suffering from notable asymmetry for OCS·Rg and for the cationic dimers with distinct terminal atoms (see also Figures S12 and S13).

For pure "linear" (nL-GS, nL-bend, nL-stre, hL-GS, hL-bend, and hL-stre) states, the largest fraction of the nuclear density is accumulated close to the terminal atoms (see Figures 8 and S14–S25). Whenever the nL- and hL-type configurations are equivalent, the nuclear density is symmetric around the two terminal atoms; otherwise, it remains only on one side of the chromophore. For the nL-stre/hL-stre states, the "doubled" density features are typically more extended along the *x* axis than the density patterns of the nL-GS and hL-GS modes.

6.3. Heavily Mixed Excited Vibrations. Due to the extremely flat PESs characterizing several dimers, the vdW bend and stretch vibrations, corresponding to the T-shaped or the linear configurations, may become strongly mixed. As a result, most bound states cannot be unambiguously assigned to a single dimer arrangement. Interaction of "nonlinear" states with "linear" ones has already been noted in refs 20, 26, 39 and 47, but this kind of mixing emerges as the general picture for several bound states in this study. In the case of the vdW combination bands, mixing is especially pronounced and is accompanied by interactions among states corresponding to the same configuration. These combination bands are not discussed here, and their density plots are available in the Supporting Information.

https://doi.org/10.1021/acs.jctc.3c00914
J. Chem. Theory Comput. 2023, 19, 8767–8781

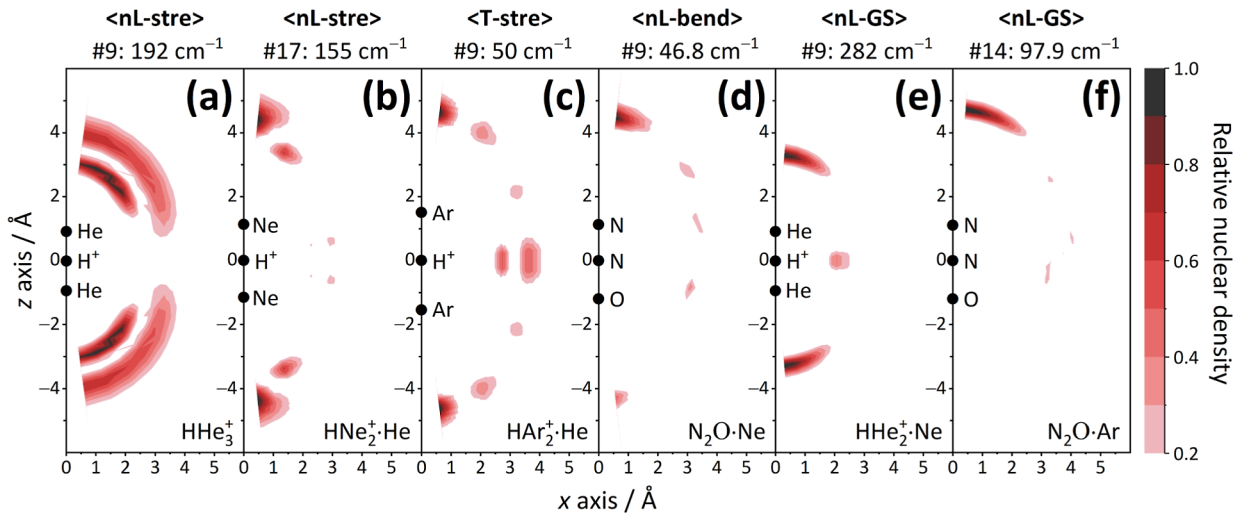

Figure 9. Nuclear densities of the solvent atoms in the *xz* plane for selected heavily mixed vdW vibrational states. For the panels of this figure, the same convention is applied as in Figure 7. Owing to the presence of strong couplings, the vibrational labels exhibited on the top of the panels are only approximate assignments. For additional details, see the caption of Figure 6.

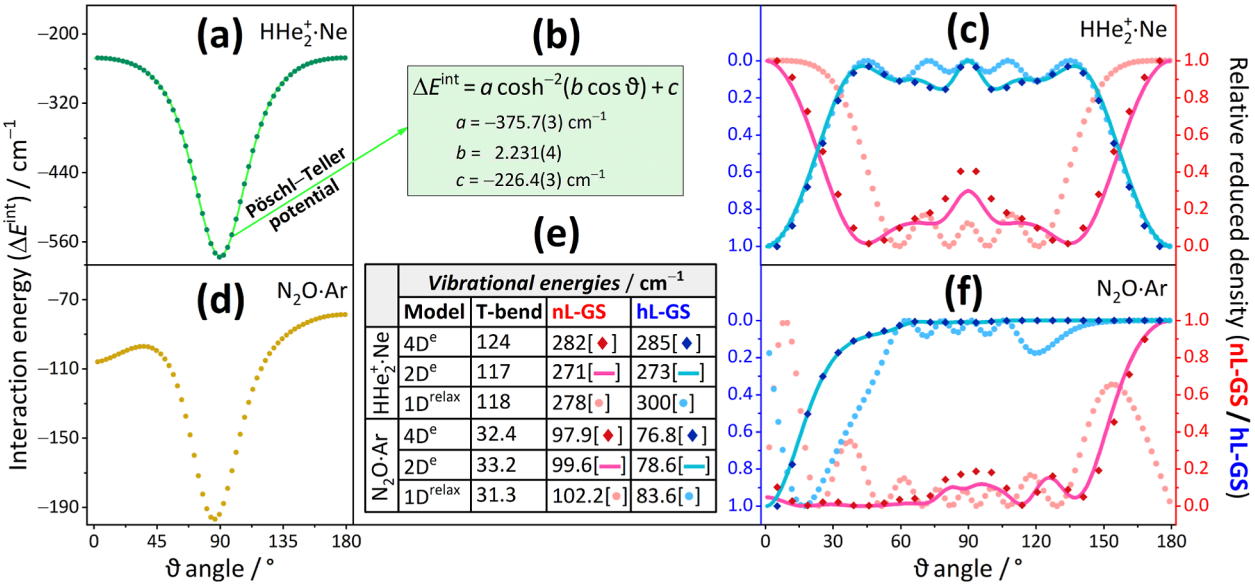

Figure 10. Illustration of nuclear-density accumulation around the linear saddle points of HHe_2^+·Ne and N_2O·Ar. For these two dimers, panels (a) and (d) display the 1D-ϑ potential, obtained from the 4D PESs by relaxing the R variable at $(\alpha, \phi) = (178°, 0°)$. The curve of panel (a) can be fitted with a Pöschl−Teller potential function,[126] whose parameters are shown in the green box of panel (b), with their last-digit uncertainties. The vibrational energies of the T-bend, nL-GS, and hL-GS states obtained with the $4D^e$, $2D^e$, and $1D^{relax}$ models are presented in panel (e) for both dimers, where $1D^{relax}$ is defined in Section 6.3. Panels (c) and (f) exhibit the reduced 1D-ϑ wave function densities derived from the three models. In the nL-GS and/or hL-GS states, all three models provide density distributions, exhibiting sharp maxima around (or at least not too far away from) the linear saddle points, that is, $\vartheta = 0°/180°$ for HHe_2^+·Ne and $\vartheta = 180°$ for N_2O·Ar. For further computational details, see the caption to Figure S26.

Figure 9 exhibits a few representative examples for strongly interacting states characterized by highly dispersive nuclear densities (for additional exotic patterns, see Figures S14−S25). As expected, mixing is strongest for the He-solvated dimers (see Figure 9a−c), but there are strong couplings for Ne- and Ar-containing complexes as well (see Figure 9d−f). The density plots presented in Figure 9a−c indicate considerable delocalization of the He atom along the z axis, in accordance with similar previous observations made for CO_2·He.[20,47] These couplings weaken for the nL-stre state when HHe_2^+ is replaced with HNe_2^+ (cf. Figure 9a,b), making the upper-left and lower-left corners shown in Figure 9b more or less similar to the density features of Figure 8i. Apparently, the significant difference is that here, (i) there is still enhanced density at the T-shaped configuration and (ii) some interaction with the nL-bend state is also present.

Among the strongly interacting vibrational states, the most noteworthy instances are those (see Figure 9e−f) where most of the nuclear density is concentrated around the linear saddle points. As a matter of fact, such states have been identified for all 13 dimers characterized by linear TSs (see Table 1); thus, these peculiar states are not computational artifacts. Upon checking the literature, a couple of ground-breaking papers[127−132] have been found, which mention the localization

https://doi.org/10.1021/acs.jctc.3c00914
J. Chem. Theory Comput. 2023, 19, 8767−8781

of nuclear wave functions at saddle points or deal with the spectroscopy of TSs, though none in the context of vdW complexes. Hence, it is worth taking a closer look at this interesting phenomenon.

For the 13 dimers with linear saddle points, 1D-ϑ wave function densities have been computed with the 4D^e, 2D^e, and 1D^{relax} models, where 1D^{relax} includes the relaxed 1D-ϑ potential and an R value fixed at $R = R_e$ in the kinetic-energy part of the vibrational Hamiltonian. The three models qualitatively produce the same vibrational energies for the T-bend, nL-GS, and hL-GS states. The results of this analysis are depicted in Figures 10 and S26−S38, suggesting that the 4D^e/3D^e and 2D^e models always produce density peaks around the linear TSs (note the reversed scale employed for the blue curves in Figure 10c,f). Therefore, it is quite surprising that no such observation was made in previous studies,[30,40,49,61,69−71,76] where 2D models were utilized to deduce vibrational states for CO_2·Ar, OCS·Ar, N_2O·Ne, and N_2O·Ar.

Five of the 13 dimers with identical terminal atoms, like HHe_2^+·Ne (see Figure 10a−c), are amenable to a description based on a Pöschl−Teller-type relaxed 1D-ϑ potential,[126] for which the 1D nuclear Schrödinger equation is exactly solvable. For these five complexes, even the simplest 1D^{relax} model is capable of reproducing the density maxima at the TSs within the nL-GS and hL-GS states (cf. Figure 10c). The situation is more involved for the other nine dimers, such as N_2O·Ar (see Figure 10d−f), where the 1D^{relax} model improperly indicates density peaks in the vicinity of both terminal atoms for the nL-GS states of linear TSs. In these cases, the inclusion of the R coordinate seems to be important, necessitating the use of at least a 2D model to retrieve the true density accumulations.

7. SUMMARY AND CONCLUSIONS

Advances in experimental spectroscopic techniques have contributed to the detailed understanding of the structures, dynamics, and vibrations of vdW complexes formed by a collection of small- and medium-sized molecules in the gas phase. Although the generation of these vdW complexes, held together by noncovalent interactions, is relatively straightforward via supersonic jet expansion methods, it is often complicated to assign their observed (ro)vibrational spectra, specifically under (ultra)high resolution. Especially in these difficult cases, highly accurate first-principles predictions are required for the correct evaluation of the experimental results.

The present theoretical study has focused on the structure, dynamics, and spectroscopy of vdW dimers containing a quasi-linear triatomic chromophore and a solvent rare-gas atom (Rg = He, Ne, and Ar). As chromophores, four neutral molecules (CO_2, CS_2, N_2O, and OCS) and six molecular ions (HHe_2^+, HNe_2^+, HAr_2^+, $HHeNe^+$, $HHeAr^+$, and $HNeAr^+$) were selected, resulting in 3 × 10 = 30 formal complexes. Our extensive electronic-structure computations revealed that (i) five cationic dimers, i.e., HHe_2^+·Ar, $HHeNe^+$·Ar, $HHeAr^+$·Ar, $HNeAr^+$·Ar, and $HHeAr^+$·Ne, do not have T-shaped minima due to an Rg ↔ Rg′ exchange, where Rg′ means the lightest rare-gas atom in the chromophore, and (ii) the T-shaped configuration is drastically less stable for HNe_2^+·Ar than its structural isomer, $HNeAr^+$·Ne. Without these six complexes, 24 dimers remain to study. These dimers were subjected to systematic first-principles computational analyses.

The approach followed in this article, combining high-level electronic-structure theory and state-of-the-art quasi-variational nuclear-motion computations based on exact kinetic-energy operators, is robust and accurate. A significant amount of computational results has been generated for the 24 dimers, helping to understand their most important structural, dynamical, and spectroscopic characteristics. The 4D PESs used in the nuclear-motion computations were constructed in a semiautomated fashion.[108,109] These accurate PESs could be utilized in various further applications, such as the modeling of spectral line shape perturbations caused by the Rg atoms in the case of the 10 linear chromophores (see, e.g., ref 133).

Our comprehensive numerical analyses demonstrate once again how effectively the intra- and intermonomer coordinates can be separated via adequate reduced-dimensional (2D to 4D) models. Based on over 1500 bound vibrational states determined, the proper view of these asymmetric-top dimers is that they behave like slightly perturbed linear molecules. The effect of the intramonomer motions on the bound-state vibrational energies is nearly constant; this provides increased accuracy when energy differences are formed, like in the case of tunneling splittings. A minimal 4D model, however, is not able to yield accurate vibrational energies for the in-plane and out-of-plane bending fundamentals of the solvated chromophores, especially in the case of the charged vdW complexes, calling for the use of more sophisticated models that account for the couplings among the intramonomer bending and stretching modes.

For the 24 dimers considered, (i) the equilibrium structures of the global minima are T-shaped, and (ii) the collinear configurations represent secondary minima or saddle points. As to the effective structures, the solvent atom, irrespective of whether it is He, Ne, or Ar, undergoes large-scale delocalization, and in the embedding chosen one always finds toroidal nuclear-density patterns. While the ground-state densities display a single uninterrupted torus, the densities of vibrationally excited states are characterized by multiple tori. The thickness of the tori changes with the size as well as the azimuthal angle of the solvating Rg atom. Although these toroidal density features have been studied only in vdW complexes, it is feasible that similar shapes occur for the torsional states of certain covalently bound T-shaped molecules.

It is an interesting though not unexpected result of this study that the expectation value of the bond angle is around 20° away from linearity for all charged chromophores, whereas the deviation is less than 10° for the neutral ones. Note, in this respect, that the Bastiansen−Morino shrinkage effect[134−136] leads to an apparent contraction of effective nonbonded distances. This shrinkage effect is especially visible in linear molecules and slightly influences the vdW vibrational energies.

Due to the extreme anharmonicity of the intermonomer modes, some of the bound vibrational states suffer from particularly strong mode mixing, making it impossible to confidently assign them to an individual (T-shaped or linear) dimer configuration. As expected, the vibrational interactions are largest for the He-solvated dimers, for which a few vibrational fundamentals fall outside the set of bound states, because of the small dissociation energies characterizing these complexes. In a somewhat counterintuitive way, certain bound states correspond to linear saddle points, an effect more or less explained by an introductory 1D model. These linear structures, which might be interpreted as metastable isomers,[129] demand further examination to give a full picture about their extraordinary dynamical behavior, in particular

https://doi.org/10.1021/acs.jctc.3c00914
J. Chem. Theory Comput. 2023, 19, 8767−8781

focusing on their ground-state-like energy levels. These additional analyses should be based on isomerization barriers, which can be derived from effective bending potentials,[132,137] and the ladder-like energy patterns of the bending overtones.[138]

Although not considered in this study, complexes where a formally linear chromophore is solvated by two or more rare-gas atoms should provide intriguing dynamical behavior and high-resolution spectra. Trimers like $HCl{\cdot}Ar_2$,[139,140] $CO_2{\cdot}Ar_2$,[141,142] and HHe_4^+ should also prove useful when the goal is to gain further insight into three-body effects, which strongly affect whether a planar or a twisted structure is realized in such molecular systems. These vdW complexes, whereby the solvent atoms implement concerted "orbiting" motions around the chromophore, will form the subject of future investigations in our group.

■ ASSOCIATED CONTENT

Data Availability Statement

A compressed archive of PES parameter files for all 24 vdW dimers (pots.zip) and a compressed archive of vibrational energies and 2D nuclear densities (vib_res.zip) are available at https://osf.io/4tzys/?view_only=5c9d8a5a653d42348fee6f11a02c678c.

Supporting Information

The Supporting Information is available free of charge at https://pubs.acs.org/doi/10.1021/acs.jctc.3c00914.

Tables S1−S10 and Figures S1−S38 (PDF)

■ AUTHOR INFORMATION

Corresponding Author

Attila G. Császár − *HUN-REN−ELTE Complex Chemical Systems Research Group, H-1518 Budapest 112, Hungary; Institute of Chemistry, ELTE Eötvös Loránd University, H-1117 Budapest, Hungary;* orcid.org/0000-0001-5640-191X; Email: attila.csaszar@ttk.elte.hu

Authors

Roland Tóbiás − *HUN-REN−ELTE Complex Chemical Systems Research Group, H-1518 Budapest 112, Hungary;* orcid.org/0000-0003-3674-5066

Irén Simkó − *Hevesy György PhD School of Chemistry and Institute of Chemistry, ELTE Eötvös Loránd University, H-1117 Budapest, Hungary*

Complete contact information is available at: https://pubs.acs.org/10.1021/acs.jctc.3c00914

Notes

The authors declare no competing financial interest.

■ ACKNOWLEDGMENTS

Financial support received through the HUN-REN Hungarian Research Network, the National Research, Development and Innovation Office (NKFIH, grants K138233 and PD145972), and the grant VEKOP-2.3.2-16-2017-00014 is gratefully acknowledged. Krzysztof Szalewicz and his group are thanked for helpful discussions related to the autoPES code. This work supports activities within the PHYMOL (Physics, Accuracy and Machine Learning: Towards the Next Generation of Molecular Potentials) project, funded mainly under the Horizon Europe scheme and also by UK Research and Innovation, and the European Cooperation in Science and Technology (COST) Action CA21101 "Confined molecular systems: from a new generation of materials to the stars (COSY)".

■ REFERENCES

(1) Császár, A. G.; Szidarovszky, T.; Asvany, O.; Schlemmer, S. Fingerprints of microscopic superfluidity in HHe_n^+ clusters. *Mol. Phys.* **2019**, *117*, 1559−1583.

(2) Asvany, O.; Schlemmer, S.; Szidarovszky, T.; Császár, A. G. Infrared signatures of the HHe_n^+ and DHe_n^+ (n = 3−6) complexes. *J. Phys. Chem. Lett.* **2019**, *10*, 5325−5330.

(3) Töpfer, M.; Jensen, A.; Nagamori, K.; Kohguchi, H.; Szidarovszky, T.; Császár, A. G.; Schlemmer, S.; Asvany, O. Spectroscopic signatures of HHe_2^+ and HHe_3^+. *Phys. Chem. Chem. Phys.* **2020**, *22*, 22885−22888.

(4) Kędziera, D.; Rauhut, G.; Császár, A. G. Structure, energetics, and spectroscopy of the chromophores of HHe^+_n, $H_2He^+_n$, and He^+_n clusters and their deuterated isotopologues. *Phys. Chem. Chem. Phys.* **2022**, *24*, 12176−12195.

(5) Simkó, I.; Schran, C.; Brieuc, F.; Fábri, C.; Asvany, O.; Schlemmer, S.; Marx, D.; Császár, A. G. Quantum nuclear delocalization and its rovibrational fingerprints. *Angew. Chem., Int. Ed.* **2023**, *62*, No. e202306744.

(6) Le Roy, R. J.; Hutson, J. M. Improved potential energy surfaces for the interaction of H_2 with Ar, Kr, and Xe. *J. Chem. Phys.* **1987**, *86*, 837−853.

(7) Steed, J. M.; Dixon, T. A.; Klemperer, W. Determination of the structure of $ArCO_2$ by radio frequency and microwave spectroscopy. *J. Chem. Phys.* **1979**, *70*, 4095−4100.

(8) DeLeon, R. L.; Muenter, J. S. Structure and properties of the argon·acetylene van der Waals molecule. *J. Chem. Phys.* **1980**, *72*, 6020−6023.

(9) Hodge, J.; Hayman, G. D.; Dyke, T. R.; Howard, B. J. Molecular-beam infrared spectroscopy of the $Ar{-}N_2O$ van der Waals molecule. *J. Chem. Soc., Faraday Trans.* **1986**, *82*, 1137−1142.

(10) Fraser, G. T.; Pine, A. S.; Suenram, R. D. Optothermal-infrared and pulsed-nozzle Fourier-transform microwave spectroscopy of rare gas−CO_2 complexes. *J. Chem. Phys.* **1988**, *88*, 6157−6167.

(11) Randall, R. W.; Walsh, M. A.; Howard, B. J. Infrared absorption spectroscopy of rare-gas−CO_2 clusters produced in supersonic expansions. *Faraday Discuss.* **1988**, *85*, 13.

(12) Sharpe, S. W.; Sheeks, R.; Wittig, C.; Beaudet, R. A. Infrared absorption spectroscopy of CO_2−Ar complexes. *Chem. Phys. Lett.* **1988**, *151*, 267−272.

(13) Fraser, G. T.; Pine, A. S. Infrared and microwave study of angular-radial coupling effects in Ar−HCN. *J. Chem. Phys.* **1989**, *91*, 3319−3326.

(14) Clary, D. C.; Dateo, C. E.; Stoecklin, T. Prediction of the spectrum for excitation of the van der Waals modes in ArHCN. *J. Chem. Phys.* **1990**, *93*, 7666−7675.

(15) Sharpe, S. W.; Reifschneider, D.; Wittig, C.; Beaudet, R. A. Infrared absorption spectroscopy of the CO_2−Ar complex in the 2376 cm^{-1} combination band region: the intermolecular bend. *J. Chem. Phys.* **1991**, *94*, 233−238.

(16) Bohac, E. J.; Marshall, M. D.; Miller, R. E. The vibrational predissociation of $Ar{-}CO_2$ at the state-to-state level. I. Vibrational propensity rules. *J. Chem. Phys.* **1992**, *97*, 4890−4900.

(17) Bemish, R. J.; Block, P. A.; Pedersen, L. G.; Yang, W.; Miller, R. E. The $Ar{-}C_2H_2$ intermolecular potential from high resolution spectroscopy and ab initio theory: a case for multicenter interactions. *J. Chem. Phys.* **1993**, *99*, 8585−8598.

(18) Bone, R. G. A. Are there geometric isomers of the van der Waals dimers Ar−OCS and $Ar{-}SO_2$? *Chem. Phys.* **1993**, *178*, 255−277.

(19) Ohshima, Y.; Matsumoto, Y.; Takami, M.; Kuchitsu, K. Free-jet infrared absorption spectroscopy of the C_2H_2−Ar complex in the doubly degenerate monomer C−H bending region. *J. Chem. Phys.* **1993**, *99*, 8385−8397.

(20) Weida, M. J.; Sperhac, J. M.; Nesbitt, D. J.; Hutson, J. M. Signatures of large amplitude motion in a weakly bound complex: high-resolution IR spectroscopy and quantum calculations for $HeCO_2$. *J. Chem. Phys.* **1994**, *101*, 8351−8363.
(21) Moszynski, R.; Wormer, P. E. S.; van der Avoird, A. Ab initio potential energy surface and near-infrared spectrum of the $He-C_2H_2$ complex. *J. Chem. Phys.* **1995**, *102*, 8385−8397.
(22) Milce, A. P.; Heard, D. E.; Miller, R. E.; Orr, B. J. Rovibrational spectroscopy of the C_2H_2·Ar van der Waals complex, using a fluorescence depletion infrared-ultraviolet double resonance technique. *Chem. Phys. Lett.* **1996**, *250*, 95−103.
(23) Bemish, R. J.; Miller, R. E. Near-infrared laser spectroscopy of the $Ar-C_2HD$ complex: Fermi resonance assisted vibrational predissociation. *Chem. Phys. Lett.* **1997**, *281*, 272−280.
(24) Yan, G.; Yang, M.; Xie, D. Ab initio potential energy surface and rovibrational spectra of $He-CO_2$. *J. Chem. Phys.* **1998**, *109*, 10284−10292.
(25) Yan, G.; Yang, M.; Xie, D. Rovibrational bound states of the Ne−OCS complex. *Chem. Phys. Lett.* **1998**, *287*, 162−168.
(26) Gianturco, F. A.; Paesani, F. The He−OCS van der Waals potential from model calculations: bound states, stable structures, and vibrational couplings. *J. Chem. Phys.* **2000**, *113*, 3011−3019.
(27) Misquitta, A. J.; Bukowski, R.; Szalewicz, K. Spectra of $Ar-CO_2$ from ab initio potential energy surfaces. *J. Chem. Phys.* **2000**, *112*, 5308−5319.
(28) Liu, Y.; Jäger, W. Isotopic study of rotational spectra of the Ar−acetylene complex. *J. Mol. Spectrosc.* **2001**, *205*, 177−182.
(29) Viel, A.; Whaley, K. B. Quantum structure and rotational dynamics of HCN in helium clusters. *J. Chem. Phys.* **2001**, *115*, 10186−10198.
(30) Zhu, H.; Xie, D.; Yan, G. Ab initio potential energy surface and rovibrational spectra of $Ne-N_2O$. *Chem. Phys. Lett.* **2002**, *351*, 149−157.
(31) Tang, J.; Xu, Y.; McKellar, A. R. W.; Jäger, W. Quantum solvation of carbonyl sulfide with helium atoms. *Science* **2002**, *297*, 2030−2033.
(32) Liu, Y.; Jäger, W. Microwave spectroscopic investigation of the Ne−acetylene van der Waals dimer. *Phys. Chem. Chem. Phys.* **2003**, *5*, 1744−1751.
(33) Xu, Y.; Jäger, W. Rotational spectroscopic investigation of carbonyl sulfide solvated with helium atoms. *J. Chem. Phys.* **2003**, *119*, 5457−5466.
(34) Xu, Y.; Jäger, W.; Tang, J.; McKellar, A. R. W. Spectroscopic studies of quantum solvation in $^4He_N-N_2O$ clusters. *Phys. Rev. Lett.* **2003**, *91*, 163401.
(35) Chang, B. T.; Akin-Ojo, O.; Bukowski, R.; Szalewicz, K. Potential energy surface and rovibrational spectrum of $He-N_2O$ dimer. *J. Chem. Phys.* **2003**, *119*, 11654−11670.
(36) Song, X.; Xu, Y.; Roy, P.-N.; Jäger, W. Rotational spectrum, potential energy surface, and bound states of the weakly bound complex $He-N_2O$. *J. Chem. Phys.* **2004**, *121*, 12308−12314.
(37) Tang, J.; McKellar, A. R. W.; Mezzacapo, F.; Moroni, S. Bridging the gap between small clusters and nanodroplets: spectroscopic study and computer simulation of carbon dioxide solvated with helium atoms. *Phys. Rev. Lett.* **2004**, *92*, 145503.
(38) Tang, J.; McKellar, A. R. W. High resolution infrared spectra of a carbon dioxide molecule solvated with helium atoms. *J. Chem. Phys.* **2004**, *121*, 181−190.
(39) Zhu, H.; Zhou, Y.; Xie, D. Ab initio intermolecular potential-energy surface and microwave spectra for the Ne−OCS complex. *J. Chem. Phys.* **2005**, *122*, 234312.
(40) Zhu, H.; Guo, Y.; Xue, Y.; Xie, D. Ab initio potential energy surface and predicted microwave spectra for Ar−OCS dimer and structures of Ar_n−OCS (n = 2−14) clusters. *J. Comput. Chem.* **2006**, *27*, 1045−1053.
(41) Abusara, Z.; Borvayeh, L.; Moazzen-Ahmadi, N.; McKellar, A. R. W. Isotope effects in the infrared spectra of OCS−He complexes and clusters. *J. Chem. Phys.* **2006**, *125*, 144306.
(42) McKellar, A. R. W. Infrared spectra of isotopic CO_2-He complexes. *J. Chem. Phys.* **2006**, *125*, 114310.
(43) McKellar, A. R. W.; Xu, Y.; Jäger, W. Spectroscopic exploration of atomic scale superfluidity in doped helium nanoclusters. *Phys. Rev. Lett.* **2006**, *97*, 183401.
(44) Topic, W.; Jäger, W.; Blinov, N.; Roy, P.-N.; Botti, M.; Moroni, S. Rotational spectrum of cyanoacetylene solvated with helium atoms. *J. Chem. Phys.* **2006**, *125*, 144310.
(45) Zhou, Y.; Xie, D.; Zhang, D. H. A three-dimensional ab initio potential energy surface and predicted infrared spectra for the $He-N_2O$ complex. *J. Chem. Phys.* **2006**, *124*, 144317.
(46) Cappelletti, D.; Bartolomei, M.; Carmona-Novillo, E.; Pirani, F.; Blanquet, G.; Thibault, F. Intermolecular interaction potentials for the $Ar-C_2H_2$, $Kr-C_2H_2$, and $Xe-C_2H_2$ weakly bound complexes: information from molecular beam scattering, pressure broadening coefficients, and rovibrational spectroscopy. *J. Chem. Phys.* **2007**, *126*, 064311.
(47) Ran, H.; Xie, D. A new potential energy surface and predicted infrared spectra of $He-CO_2$: dependence on the antisymmetric stretch of CO_2. *J. Chem. Phys.* **2008**, *128*, 124323.
(48) Li, H.; Le Roy, R. J. Analytic three-dimensional 'MLR' potential energy surface for CO_2-He, and its predicted microwave and infrared spectra. *Phys. Chem. Chem. Phys.* **2008**, *10*, 4128−4137.
(49) Cui, Y.; Ran, H.; Xie, D. A new potential energy surface and predicted infrared spectra of the $Ar-CO_2$ van der Waals complex. *J. Chem. Phys.* **2009**, *130*, 224311.
(50) Lauzin, C.; Didriche, K.; Macko, P.; Demaison, J.; Liévin, J.; Herman, M. $^{12}C_2H_2-Ar$ van der Waals complex. *J. Phys. Chem. A* **2009**, *113*, 2359−2365.
(51) Seal, P.; Chakrabarti, S. Suitability of double hybrid density functionals and their dispersion-corrected couterparts in producing the potential energy curves for of CO_2-Rg (Rg: He, Ne, Ar and Kr) systems. *J. Phys. Chem. A* **2009**, *113*, 1377−1383.
(52) Chen, R.; Jiao, E.; Zhu, H.; Xie, D. A new ab initio potential energy surface and microwave and infrared spectra for the $Ne-CO_2$ complex. *J. Chem. Phys.* **2010**, *133*, 104302.
(53) Didriche, K.; Földes, T.; Lauzin, C.; Golebiowski, D.; Liévin, J.; Herman, M. Experimental 2CH excitation in acetylene-containing van der Waals complexes. *Mol. Phys.* **2012**, *110*, 2781−2796.
(54) Li, H.; Ma, Y.-T. An intramolecular vibrationally excited intermolecular potential for He−OCS: globally tested by simulation of vibrational shifts for OCS in He_N N = 1−100 clusters. *J. Chem. Phys.* **2012**, *137*, 234310.
(55) Rezaei, M.; Moazzen-Ahmadi, N.; McKellar, A. R. W.; Fernández, B.; Farrelly, D. Towards an understanding of the helium-acetylene van der Waals complex. *Mol. Phys.* **2012**, *110*, 2743−2750.
(56) Wang, L.; Xie, D.; Le Roy, R. J.; Roy, P.-N. A new four-dimensional ab initio potential energy surface for N_2O-He and vibrational band origin shifts for the N_2O-He_N clusters with N = 1−40. *J. Chem. Phys.* **2012**, *137*, 104311.
(57) Lauzin, C.; Coudert, L. H.; Herman, M.; Liévin, J. Ab initio intermolecular potential of $Ar-C_2H_2$ refined using high-resolution spectroscopic data. *J. Phys. Chem. A* **2013**, *117*, 13767−13774.
(58) Wang, Z.; Feng, E.; Zhang, C.; Sun, C. A new potential energy surface and microwave and infrared spectra of the He−OCS complex. *J. Chem. Phys.* **2014**, *141*, 174308.
(59) Yuan, T.; Sun, X.; Hu, Y.; Zhu, H. A new ab initio potential energy surface and infrared spectra for the $Ar-CS_2$ complex. *J. Chem. Phys.* **2014**, *141*, 104306.
(60) Zang, L.; Dai, W.; Zheng, L.; Duan, C.; Lu, Y.; Yang, M. Theoretical prediction of the linear isomers for rare gas-carbon disulfide complexes: $He-CS_2$, $Ne-CS_2$, and $Ar-CS_2$. *J. Chem. Phys.* **2014**, *140*, 114310.
(61) Sun, C.; Wang, Z.; Feng, E.; Zhang, C. A three-dimensional potential energy surface and infrared spectra for the Ar−OCS van der Waals complex. *Chem. Phys. Lett.* **2014**, *592*, 182−187.

https://doi.org/10.1021/acs.jctc.3c00914
J. Chem. Theory Comput. 2023, 19, 8767−8781

(62) Hu, Y.; Yuan, T.; Zhu, H. A new ab initio potential energy surface and infrared spectra for the Ne−CS_2 complex. *Comput. Theor. Chem.* **2015**, *1056*, 47−51.
(63) Moazzen-Ahmadi, N.; McKellar, A. R. W.; Fernández, B.; Farrelly, D. The infrared spectrum of the He−C_2D_2 complex. *J. Chem. Phys.* **2015**, *142*, 084312.
(64) Shang, J.; Yuan, T.; Zhu, H. A new four-dimensional potential energy surface of the Ar−CS_2 complex: dependence on the symmetric and antisymmetric stretching vibrations of CS_2. *Chem. Phys. Lett.* **2016**, *648*, 147−151.
(65) Shang, J.; Yuan, T.; Zhu, H. A new four-dimensional ab initio potential energy surface and predicted infrared spectra for the He−CS_2 complex. *Theor. Chem. Acc.* **2016**, *135*, 1−8.
(66) Wang, Z.; Feng, E.; Zhang, C.; Sun, C. The potential energy surface and infrared spectra of the Ar−C_2H_2 complex. *Comput. Theor. Chem.* **2017**, *1112*, 82−87.
(67) Lv, J.; Wang, H.; Zheng, L.; Yang, D.; Zheng, R. An accurate prediction of the infrared spectra for Rg−CS_2 (Rg = He, Ne, Ar) complexes in the $\nu_1 + \nu_3$ region of CS_2 monomer. *Chem. Phys. Lett.* **2017**, *687*, 31−37.
(68) Qin, M.; Shang, J.; Hong, Q.; Zhu, H. A new four-dimensional ab initio potential energy surface and predicted infrared spectra for the Ne−CS_2 complex. *Mol. Phys.* **2017**, *115*, 379−385.
(69) Zhao, A.; Shi, L.; Tian, Y.; Zheng, L.; Zheng, R. Theoretical studies for the infrared spectra of Ar−CO_2 complex: fundamental and combination bands. *Spectrochim. Acta, Part A* **2018**, *204*, 308−316.
(70) Zhang, C.; Sun, C.; Han, Y.; Wang, Z. The weakly bound Ar−N_2O complex: a new potential energy surface and microwave spectrum. *Comput. Theor. Chem.* **2018**, *1141*, 41−44.
(71) Shi, L.; Zhao, A.; Wang, H.; Tian, Y.; Zheng, R. Theoretical study of infrared spectra for the Ar−N_2O complex: fundamental and combination bands. *J. Mol. Spectrosc.* **2019**, *357*, 24−31.
(72) Gartner, T. A.; Barclay, A. J.; McKellar, A. R. W.; Moazzen-Ahmadi, N. Symmetry breaking of the bending mode of CO_2 in the presence of Ar. *Phys. Chem. Chem. Phys.* **2020**, *22*, 21488−21493.
(73) Zhao, A.; Shi, L.; Tian, Y.; Yang, D.; Zheng, R. Investigating the spectroscopic characteristics of twelve isotopologues for the Ar−CO_2 complex. *J. Quant. Spectrosc. Radiat. Transfer* **2020**, *242*, 106778.
(74) Barclay, A. J.; McKellar, A. R. W.; Moazzen-Ahmadi, N. New infrared spectra of CO_2−Ne: fundamental for CO_2−^{22}Ne isotopologue, intermolecular bend, and symmetry breaking of the intramolecular CO_2 bend. *Chem. Phys. Lett.* **2021**, *779*, 138874.
(75) Barclay, A. J.; McKellar, A. R. W.; Western, C. M.; Moazzen-Ahmadi, N. New infrared spectra of CO_2−Xe: modelling Xe isotope effects, intermolecular bend and stretch, and symmetry breaking of the CO_2 bend. *Mol. Phys.* **2021**, *119*, No. e1919325.
(76) Sode, O.; Ruiz, J.; Peralta, S. Theoretical investigation of the vibrational structure of the Ar−CO_2 complex. *J. Mol. Spectrosc.* **2021**, *380*, 111512.
(77) Gergess, C.; Dehghany, M.; Michaelian, K. H.; McKellar, A. R. W.; Moazzen-Ahmadi, N. N_2O−Ar and N_2O−Kr: intermolecular vibrations of N_2O−Kr and symmetry breaking of the N_2O bending mode in the presence of a rare gas. *J. Mol. Spectrosc.* **2022**, *383*, 111551.
(78) Draeger, E. W.; Ceperley, D. M. Superfluidity in a doped helium droplet. *Phys. Rev. Lett.* **2003**, *90*, 065301.
(79) Toennies, J. P. Helium clusters and droplets: microscopic superfluidity and other quantum effects. *Mol. Phys.* **2013**, *111*, 1879−1891.
(80) Borocci, S.; Grandinetti, F.; Sanna, N. On the proton-bound noble gas dimers $(Ng−H−Ng)^+$ and $(Ng−H−Ng')^+$ (Ng, Ng′ = He−Xe): relationships between structure, stability, and bonding character. *Molecules* **2021**, *26*, 1305.
(81) Tan, J. A.; Kuo, J.-L. Spectral signatures of protonated noble gas clusters of Ne, Ar, Kr, and Xe: from monomers to trimers. *Molecules* **2022**, *27*, 3198.
(82) Barlow, M. J.; Swinyard, B. M.; Owen, P. J.; Cernicharo, J.; Gomez, H. L.; Ivison, R. J.; Krause, O.; Lim, T. L.; Matsuura, M.; Miller, S.; Olofsson, G.; Polehampton, E. T. Detection of a noble gas molecular ion, $^{36}ArH^+$, in the Crab Nebula. *Science* **2013**, *342*, 1343−1345.
(83) Schilke, P.; Neufeld, D. A.; Müller, H. S. P.; Comito, C.; Bergin, E. A.; Lis, D. C.; Gerin, M.; Black, J. H.; Wolfire, M.; Indriolo, N.; Pearson, J. C.; Menten, K. M.; Winkel, B.; Sánchez-Monge, Á.; Möller, T.; Godard, B.; Falgarone, E. Ubiquitous argonium (ArH^+) in the diffuse interstellar medium: a molecular tracer of almost purely atomic gas. *Astron. Astrophys.* **2014**, *566*, A29.
(84) Müller, H. S. P.; Muller, S.; Schilke, P.; Bergin, E. A.; Black, J. H.; Gerin, M.; Lis, D. C.; Neufeld, D. A.; Suri, S. Detection of extragalactic argonium, ArH^+, toward PKS 1830−211. *Astron. Astrophys.* **2015**, *582*, L4.
(85) Güsten, R.; Wiesemeyer, H.; Neufeld, D.; Menten, K. M.; Graf, U. U.; Jacobs, K.; Klein, B.; Ricken, O.; Risacher, C.; Stutzki, J. Astrophysical detection of the helium hydride ion HeH^+. *Nature* **2019**, *568*, 357−359.
(86) McDonald, D.; Mauney, D.; Leicht, D.; Marks, J.; Tan, J.; Kuo, J.-L.; Duncan, M. Communication: trapping a proton in argon: spectroscopy and theory of the proton-bound argon dimer and its solvation. *J. Chem. Phys.* **2016**, *145*, 231101.
(87) Denis-Alpizar, O.; Cabrera-González, L. D.; Páez-Hernández, D.; Pino-Rios, R. Quantum inelastic scattering of $ArHAr^+$, $HeHHe^+$, and $NeHNe^+$ with He on new potential energy surfaces. *ACS Earth Space Chem.* **2022**, *6*, 1924−1929.
(88) Denis-Alpizar, O.; Cabrera-González, L. D.; Orellana-González, G.; Páez-Hernández, D. Rotational state-to-state rate coefficients of $HeHNe^+$ by collision with He at low temperatures. *ACS Earth Space Chem.* **2023**, *7*, 212−217.
(89) Stone, A. J. *The Theory of Intermolecular Forces*, 2nd ed.; Oxford University Press: Oxford, 2013.
(90) Toczyłowski, R. R.; Doloresco, F.; Cybulski, S. M. Theoretical study of the He−HCN, Ne−HCN, Ar−HCN, and Kr−HCN complexes. *J. Chem. Phys.* **2001**, *114*, 851−864.
(91) Wilson, E. B., Jr.; Decius, J. C.; Cross, P. C. *Molecular Vibrations: The Theory of Infrared and Raman Vibrational Spectra*; McGraw Hill: New York, 1955.
(92) Nielsen, H. H. The vibration-rotation energies of molecules. *Rev. Mod. Phys.* **1951**, *23*, 90−136.
(93) Clabo, D. A.; Allen, W. D.; Remington, R. B.; Yamaguchi, Y.; Schaefer, H. F. A systematic study of molecular vibrational anharmonicity and vibration−rotation interaction by self-consistent-field higher derivative methods. Asymmetric top molecules. *Chem. Phys.* **1988**, *123*, 187−239.
(94) Allen, W. D.; Yamaguchi, Y.; Császár, A. G.; Clabo, D. A., Jr.; Remington, R. B.; Schaefer, H. F., III A systematic study of molecular vibrational anharmonicity and vibration-rotation interaction by self-consistent-field higher derivative methods. Linear polyatomic molecules. *Chem. Phys.* **1990**, *145*, 427−466.
(95) Császár, A. G.; Fábri, C.; Szidarovszky, T.; Mátyus, E.; Furtenbacher, T.; Czakó, G. The fourth age of quantum chemistry: molecules in motion. *Phys. Chem. Chem. Phys.* **2012**, *14*, 1085−1106.
(96) Simkó, I.; Fábri, C.; Császár, A. G. Quantum-chemical and quantum-graph models of the dynamical structure of CH_5^+. *J. Chem. Theory Comput.* **2023**, *19*, 42−50.
(97) Møller, C.; Plesset, M. S. Note on an approximation treatment for many-electron systems. *Phys. Rev.* **1934**, *46*, 618−622.
(98) Raghavachari, K.; Trucks, G. W.; Pople, J. A.; Head-Gordon, M. A fifth-order perturbation comparison of electron correlation theories. *Chem. Phys. Lett.* **1989**, *157*, 479−483.
(99) Dunning, T. H., Jr. Gaussian basis sets for use in correlated molecular calculations. I. The atoms boron through neon and hydrogen. *J. Chem. Phys.* **1989**, *90*, 1007−1023.
(100) Allen, W. D.; Császár, A. G. On the ab initio determination of higher-order force constants at nonstationary reference geometries. *J. Chem. Phys.* **1993**, *98*, 2983−3015.
(101) Tóbiás, R.; Árendás, P.; Császár, A. G. Normal-mode vibrational analysis of weakly bound oligomers at constrained stationary points of arbitrary order. *J. Chem. Theory Comput.* **2022**, *18*, 1788−1798.

https://doi.org/10.1021/acs.jctc.3c00914
J. Chem. Theory Comput. 2023, 19, 8767−8781

(102) Fukui, K. Formulation of the reaction coordinate. *J. Phys. Chem.* **1970**, *74*, 4161−4163.
(103) Fukui, K. The path of chemical reactions—the IRC approach. *Acc. Chem. Res.* **1981**, *14*, 363−368.
(104) Frisch, M. J.; Trucks, G. W.; Schlegel, H. B.; Scuseria, G. E.; Robb, M. A.; Cheeseman, J. R.; Scalmani, G.; Barone, V.; Petersson, G. A.; Nakatsuji, H.; Li, X.; Caricato, M.; Marenich, A. V.; Bloino, J.; Janesko, B. G.; Gomperts, R.; Mennucci, B.; Hratchian, H. P.; Ortiz, J. V.; Izmaylov, A. F.; Sonnenberg, J. L.; Williams-Young, D.; Ding, F.; Lipparini, F.; Egidi, F.; Goings, J.; Peng, B.; Petrone, A.; Henderson, T.; Ranasinghe, D.; Zakrzewski, V. G.; Gao, J.; Rega, N.; Zheng, G.; Liang, W.; Hada, M.; Ehara, M.; Toyota, K.; Fukuda, R.; Hasegawa, J.; Ishida, M.; Nakajima, T.; Honda, Y.; Kitao, O.; Nakai, H.; Vreven, T.; Throssell, K.; Montgomery, J. A.; Peralta, J. E.; Ogliaro, F.; Bearpark, M. J.; Heyd, J. J.; Brothers, E. N.; Kudin, K. N.; Staroverov, V. N.; Keith, T. A.; Kobayashi, R.; Normand, J.; Raghavachari, K.; Rendell, A. P.; Burant, J. C.; Iyengar, S. S.; Tomasi, J.; Cossi, M.; Millam, J. M.; Klene, M.; Adamo, C.; Cammi, R.; Ochterski, J. W.; Martin, R. L.; Morokuma, K.; Farkas, O.; Foresman, J. B.; Fox, D. J. *Gaussian 16*, Revision B.01; Gaussian Inc.: Wallingford CT, 2016.
(105) Császár, A. G. Anharmonic molecular force fields. *Wiley Interdiscip. Rev.: Comput. Mol. Sci.* **2012**, *2*, 273−289.
(106) Matthews, D. A.; Cheng, L.; Harding, M. E.; Lipparini, F.; Stopkowicz, S.; Jagau, T.-C.; Szalay, P. G.; Gauss, J.; Stanton, J. F. Coupled-cluster techniques for computational chemistry: the CFOUR program package. *J. Chem. Phys.* **2020**, *152*, 214108.
(107) CFOUR, a quantum chemical program package. 2020. https://www.cfour.deweb/.
(108) Metz, M. P.; Piszczatowski, K.; Szalewicz, K. Automatic generation of intermolecular potential energy surfaces. *J. Chem. Theory Comput.* **2016**, *12*, 5895−5919.
(109) Metz, M. P.; Szalewicz, K. Automatic generation of flexible-monomer intermolecular potential energy surfaces. *J. Chem. Theory Comput.* **2020**, *16*, 2317−2339.
(110) Bukowski, R.; Cencek, W.; Jankowski, P.; Jeziorska, M.; Jeziorski, B.; Korona, T.; Kucharski, S. A.; Lotrich, V. F.; Misquitta, A. J.; Moszynski, R.; Patkowski, K.; Podeszwa, R.; Rybak, S.; Szalewicz, K.; Williams, H. L.; Wheatley, R. J.; Wormer, P. E. S.; Zuchowski, P. S. *SAPT2016: An Ab Initio Program for Symmetry-Adapted Perturbation Theory*, 2016.
(111) Garcia, J.; Podeszwa, R.; Szalewicz, K. SAPT codes for calculations of intermolecular interaction energies. *J. Chem. Phys.* **2020**, *152*, 184109.
(112) MOLPRO website. 2020. https://www.molpro.netweb/.
(113) Neese, F.; Wennmohs, F.; Becker, U.; Riplinger, C. The ORCA quantum chemistry program package. *J. Chem. Phys.* **2020**, *152*, 224108.
(114) Boys, S. F.; Bernardi, F. The calculation of small molecular interactions by the differences of separate total energies. Some procedures with reduced errors. *Mol. Phys.* **1970**, *19*, 553−566.
(115) Akin-Ojo, O.; Bukowski, R.; Szalewicz, K. Ab initio studies of He−HCCCN interaction. *J. Chem. Phys.* **2003**, *119*, 8379−8396.
(116) Helgaker, T.; Klopper, W.; Koch, H.; Noga, J. Basis-set convergence of correlated calculations on water. *J. Chem. Phys.* **1997**, *106*, 9639−9646.
(117) Jeziorski, B.; Moszynski, R.; Szalewicz, K. Perturbation theory approach to intermolecular potential energy surfaces of van der Waals complexes. *Chem. Rev.* **1994**, *94*, 1887−1930.
(118) Mátyus, E.; Czakó, G.; Császár, A. G. Toward black-box-type full- and reduced-dimensional variational (ro)vibrational computations. *J. Chem. Phys.* **2009**, *130*, 134112.
(119) Fábri, C.; Mátyus, E.; Császár, A. G. Rotating full- and reduced-dimensional quantum chemical models of molecules. *J. Chem. Phys.* **2011**, *134*, 074105.
(120) Fábri, C.; Quack, M.; Császár, A. G. On the use of nonrigid-molecular symmetry in nuclear-motion computations employing a discrete variable representation: a case study of the bending energy levels of CH_5^+. *J. Chem. Phys.* **2017**, *147*, 134101.
(121) Harris, D. O.; Engerholm, G. G.; Gwinn, W. D. Calculation of matrix elements for one-dimensional quantum-mechanical problems and the application to anharmonic oscillators. *J. Chem. Phys.* **1965**, *43*, 1515−1517.
(122) Harris, F. E. *Mathematics for Physical Science and Engineering: Symbolic Computing Applications in Maple and Mathematica*; Academic Press, 2014.
(123) Beyer, M.; Lammers, A.; Savchenko, E. V.; Niedner-Schatteburg, G.; Bondybey, V. E. Proton solvated by noble-gas atoms: simplest case of a solvated ion. *Phys. Chem. Chem. Phys.* **1999**, *1*, 2213−2221.
(124) Singh, U. C.; Kollman, P. A. An approach to computing electrostatic charges for molecules. *J. Comput. Chem.* **1984**, *5*, 129−145.
(125) Besler, B. H.; Merz, K. M.; Kollman, P. A. Atomic charges derived from semiempirical methods. *J. Comput. Chem.* **1990**, *11*, 431−439.
(126) Pöschl, G.; Teller, E. Bemerkungen zur Quantenmechanik des anharmonischen Oszillators. *Z. Phys.* **1933**, *83*, 143−151.
(127) Moiseyev, N. On the "New possibility of chemical bonding": anti-resonance phenomena. *Chem. Phys. Lett.* **1984**, *106*, 354−355.
(128) Dutta, P.; Bhattacharyya, S. P. Localized quantum states on and above the top of a barrier. *Phys. Lett. A* **1992**, *163*, 193−198.
(129) Henderson, J. R.; Lam, H. A.; Tennyson, J. Highly excited vibrational states of the KCN molecule. *J. Chem. Soc., Faraday Trans.* **1992**, *88*, 3287−3293.
(130) Rhodes, C. J.; Macrae, R. M. "Vibrational bonding": a new type of chemical bond is discovered. *Sci. Prog.* **2015**, *98*, 12−33.
(131) Baraban, J. H.; Changala, P. B.; Mellau, G. C.; Stanton, J. F.; Merer, A. J.; Field, R. W. Spectroscopic characterization of isomerization transition states. *Science* **2015**, *350*, 1338−1342.
(132) Mellau, G. C.; Kyuberis, A. A.; Polyansky, O. L.; Zobov, N.; Field, R. W. Saddle point localization of molecular wavefunctions. *Sci. Rep.* **2016**, *6*, 33068.
(133) Salem, J.; Tóbiás, R.; Császár, A. G.; Al-Mogren, M. M.; Jaidane, N.-E.; Hochlaf, M. Temperature-dependent line-broadening effects in CO_2 caused by Ar. *ChemPhysChem* **2023**, *24*, e202300467.
(134) Morino, Y. The effect of thermal vibration of gaseous molecules in electron diffraction studies. *Acta Crystallogr.* **1960**, *13*, 1107.
(135) Bastiansen, O.; Trætteberg, M. The influence of thermal motion on structure determination of linear molecules using the electron-diffraction method. *Acta Crystallogr.* **1960**, *13*, 1108.
(136) Morino, Y.; Cyvin, S. J.; Kuchitsu, K.; Iijima, T. Shrinkage effect for nonlinear conformations. *J. Chem. Phys.* **1962**, *36*, 1109−1110.
(137) Borondo, F.; Zembekov, A.; Benito, R. Quantum manifestations of saddle-node bifurcations. *Chem. Phys. Lett.* **1995**, *246*, 421−426.
(138) Mellau, G. C. Complete experimental rovibrational eigenenergies of HCN up to 6880 cm^{-1} above the ground state. *J. Chem. Phys.* **2011**, *134*, 234303.
(139) Elrod, M. J.; Steyert, D. W.; Saykally, R. J. Tunable far infrared-laser spectroscopy of a ternary van der Waals cluster Ar_2HCl—a sensitive probe of 3-body forces. *J. Chem. Phys.* **1991**, *94*, 58−66.
(140) Elrod, M. J.; Steyert, D. W.; Saykally, R. J. An investigation of 3-body effects in intermolecular forces. 2. Far-infrared vibration-rotation tunneling laser spectroscopy of Ar_2HCl. *J. Chem. Phys.* **1991**, *95*, 3182−3190.
(141) Xu, Y. J.; Jager, W.; Gerry, M. C. L. Pulsed molecular beam microwave Fourier transform spectroscopy of the van der Waals trimer $Ar_2−CO_2$. *J. Mol. Spectrosc.* **1993**, *157*, 132−140.
(142) Sperhac, J. M.; Weida, M. J.; Nesbitt, D. J. Infrared spectroscopy of Ar_2CO_2 trimer: vibrationally averaged structures, solvent shifts, and three-body effects. *J. Chem. Phys.* **1996**, *104*, 2202−2213.

https://doi.org/10.1021/acs.jctc.3c00914
J. Chem. Theory Comput. 2023, 19, 8767−8781